Article

Cellular Contraction and Polarization Drive Collective Cellular Motion

Jacob Notbohm,[1,2] Shiladitya Banerjee,[3] Kazage J. C. Utuje,[4] Bomi Gweon,[1,5] Hwanseok Jang,[6] Yongdoo Park,[6] Jennifer Shin,[7] James P. Butler,[1,8] Jeffrey J. Fredberg,[1,*] and M. Cristina Marchetti[4,*]

[1]Harvard T. H. Chan School of Public Health, Boston, Massachusetts; [2]Department of Engineering Physics, University of Wisconsin-Madison, Madison, Wisconsin; [3]James Franck Institute, The University of Chicago, Chicago, Illinois; [4]Department of Physics and Syracuse Biomaterials Institute, Syracuse University, Syracuse, New York; [5]Department of Biomedical Engineering, Hanyang University, Seoul, Korea; [6]Department of Biomedical Engineering, Korea University, Seoul, Korea; [7]Department of Mechanical Engineering, KAIST, Daejeon, Korea; and [8]Department of Medicine, Harvard Medical School and Brigham and Women's Hospital, Boston, Massachusetts

ABSTRACT   Coordinated motions of close-packed multicellular systems typically generate cooperative packs, swirls, and clusters. These cooperative motions are driven by active cellular forces, but the physical nature of these forces and how they generate collective cellular motion remain poorly understood. Here, we study forces and motions in a confined epithelial monolayer and make two experimental observations: 1) the direction of local cellular motion deviates systematically from the direction of the local traction exerted by each cell upon its substrate; and 2) oscillating waves of cellular motion arise spontaneously. Based on these observations, we propose a theory that connects forces and motions using two internal state variables, one of which generates an effective cellular polarization, and the other, through contractile forces, an effective cellular inertia. In agreement with theoretical predictions, drugs that inhibit contractility reduce both the cellular effective elastic modulus and the frequency of oscillations. Together, theory and experiment provide evidence suggesting that collective cellular motion is driven by at least two internal variables that serve to sustain waves and to polarize local cellular traction in a direction that deviates systematically from local cellular velocity.

INTRODUCTION

During wound repair, embryonic development, and cancer invasion, cells migrate in cooperative packs (1–3) that generate swirls (4,5) and waves (6,7). Our understanding of how cellular forces generate these collective behaviors is limited, but recent experiments have offered some clues. First, within a confluent monolayer cells tend to migrate along orientations of minimal intercellular shear stress (8–10); cell-cell junctions along these orientations carry appreciable normal stresses but only minimal shear stresses. Second, far from any boundary, each cell exerts local tractions upon its substrate that tend to align with the direction of local motion (8,11); near a boundary, by contrast, tractions tend to align systematically toward the cell-free boundary regardless of the direction of local cellular motion (11).

Some previous theoretical models (12–15), but not all (16), have recognized that local tractions can align in a di-

rection that deviates transiently, but not systematically, from that of the local velocity. This transient misalignment has been modeled by introducing noisy fluctuations around a tendency toward realignment (15,17) or via an internal variable that regulates the correlation between traction and velocity (12–14). Here, we provide further evidence that each cell polarizes so as to apply local traction in a direction that can deviate systematically from its local velocity, and that this systematic deviation is a general property of collective cellular motion. If local traction and local velocity are not aligned, it follows logically that tractions cannot result solely from viscous friction between the moving cell and its motionless substrate; rather, tractions must be regulated by variables in addition to velocity (12–14).

To identify state variables that control cellular motion and propulsive forces, we study oscillating collective waves of cellular motion that are known to arise spontaneously in a confined epithelial monolayer (7). Oscillations in passive mechanical systems result from the exchange of elastic potential energy and inertial kinetic energy. Previous work has established that cell layers behave elastically (6) but have negligible inertia (13–15). To account for the collective

oscillations of cellular motion, we therefore propose an internal variable that provides an effective inertia in the sense that it sets a timescale for turnover in intracellular contractile tension (14). To account for the local angular deviation between cell traction and velocity, we propose a second internal variable that we call cell polarization. Using a minimal physical model, we show that these two internal state variables account for both the experimentally observed oscillatory waves of motion and local systematic angular deviation between cell traction and velocity. We conclude that the collective modes of cellular motion result from an interplay between cell contraction and polarization.

MATERIALS AND METHODS

Cell culture

Madin-Darbvy canine kidney type II cells, expressing GFP with a nuclear localization signal (pAcGFP1-Nuc vector, Clontech), were supplied by A. Pegoraro and D. Weitz (Harvard University). The cells were maintained in low-glucose Dulbecco's modified Eagle's medium (12320-032; Life Technologies, Carlsbad, CA) with 10% fetal bovine serum (Corning) and 1% penicillin-streptomycin (Sigma-Aldrich. St. Louis, MO) in an incubator at 37°C and 5% CO_2.

Preparation of polyacrylamide substrates

Polyacrylamide gels with Young's modulus of 6 kPa and thickness of 100 μm were polymerized by preparing a solution of 5.5% weight/volume (w/v) acrylamide (Biorad Laboratories, Hercules, CA), 0.20% w/v bisacrylamide (Biorad Laboratories), 0.014% w/v fluorescent particles (diameter 0.5 μm, carboxylate-modified; Life Technologies), 0.05% w/v ammonium persulfate (Biorad Laboratories), and 1/2000 volume/volume TEMED (Biorad Laboratories). The gel solution was pipetted onto no. 1.5 glass bottom dishes (In Vitro Scientific, Mountain View, CA), a glass coverslip (no. 1 thickness, 18-mm diameter circle) was placed on top, and the dishes were centrifuged upside down so that the fluorescent particles collected at the top surface of the gel. The gels were functionalized with type 1 rat tail collagen (BD Biosciences, Franklin Lakes, NJ; 0.01 mg/mL, 1 mL per 18-mm diameter gel) using the covalent cross-linker sulfo-SANPAH (Pierce Biotechnology, Waltham, MA) as described previously (18).

Micropatterning expanding and confined cellular islands

Masks were prepared with circular holes (diameter 700 μm) using standard techniques in soft lithography similar to those described previously (6). Silicon-photoresist masters were custom fabricated (MicroFit, Seongnam-si, Gyeonggi-do, Korea), and polydimethylsiloxane (PDMS) (Sylgard 184, Dow Corning, Midland, MI) was poured onto the masters to cure overnight on a hot plate at 80°C. The PDMS masks were sterilized with 70% ethanol and incubated at 37°C in 2% Pluronic F-127 (Sigma-Aldrich) for 4 h to prevent cell adhesion to the masks. For expanding islands, masks were placed on the collagen-coated polyacrylamide gels, and a 200 μL droplet of cell suspension (4×10^5 cells total) was placed on each mask. The gels were transferred to a 37°C/5% CO_2 incubator for 45 min for the cells to adhere to the collagen. Afterward, the 200 μL droplets were aspirated off of the PDMS masks, the masks were removed with tweezers, and the gels were rinsed with phosphate-buffered saline (PBS) before addition of 3 mL fresh medium. For confined islands, masks were placed onto the polyacrylamide

gels before functionalizing with collagen, thus leaving a circular island of collagen to which the cells adhered. Imaging of the cell monolayers began approximately 1 h after seeding and continued for ~30 h.

Microscopy

Images of the cells, nuclei, and beads were captured every 20 min using phase-contrast (for cells) or fluorescent (for nuclei and beads) microscopy using a DMI6000B microscope with a 5× NA 0.12 objective and a DFC345FX CCD camera (Leica Microsystems, Wetzlar, Germany). Fluorescent particles and cell nuclei were imaged with fluorescence; cells were imaged with phase contrast. The imaging environment was maintained at 37°C/5% CO_2 in a heated enclosure (PeCon, Erbach, Germany). For experiments with expanding cellular islands a 2×2 grid of images was captured and stitched together using the freely available Fiji distribution of ImageJ (http://fiji.sc/Fiji) (19). After each time-lapse experiment, cells were removed from the polyacrylamide substrates by incubating in 0.05% trypsin for 20 min, and images of the fluorescent particles were collected; these images captured a stress-free reference state of the polyacrylamide substrates for subsequent computation of tractions.

Measuring cell velocity and rate-of-strain

The velocity fields were measured using custom particle image velocimetry (also called digital image correlation) software of phase contrast images written in Matlab (The Mathworks, Natick, MA). Interrogation windows of 64×64 pixels were used; this window size allowed for a spatial resolution of ~16 pixels (14 μm). Boundaries of the cell islands were detected automatically using a previously described protocol (20). The rate-of-strain tensor was computed by numerically differentiating the velocity fields in space.

Traction force microscopy and monolayer stress microscopy

Displacements of the particles were measured using digital image correlation, and tractions exerted between the cell layer and its substrate were computed using unconstrained Fourier transform traction microscopy (21) taking into account the effects of finite substrate thickness (18,22). From these measured tractions we computed the distribution of internal stresses within the cell layer using monolayer stress microscopy (MSM) (8,23).

MSM rests upon the main assumptions that the cell layer is flat, continuous and thin. Regardless of material properties of the cell layer, including any effects of nonlinearity and viscoelasticity, Newton's laws in one dimension demand that these internal stresses and boundary traction stresses must always remain in precise balance, and the MSM solution in that case is therefore exact (8,23). In two dimensions, matters are slightly more complicated, because the Poisson effect makes the solution inexact. Nevertheless, the sensitivity to the Poisson effect has been shown to be quite small, and the solution has been shown to be insensitive to a remarkably wide range of assumptions about material properties of the cell layer itself, its nonlinearity, and its viscoelasticity (8,23); this finding was further validated independently by Zimmermann et al. (17), who used a particle-based simulation to show that the stresses in the simulation are recovered by MSM with a high degree of accuracy. In two dimensions, three independent components of the stress tensor within the monolayer are obtained by solving three coupled equations. Two of those equations describe force balance, making no assumptions about the properties of the monolayer (8,23). The third equation is the compatibility of the deformation field. (For more information, see the Supporting Material.) Displacements, tractions, and stresses are measured at the same spatial resolution as the velocity field, 14 μm.

Measuring cell area and density

The position of each cell's nucleus was computed from the fluorescent images of nuclei using the watershed transform in Matlab. For each cell, the distance between its nucleus and the nuclei of the nearest six neighbors was computed and averaged; this distance was taken to be the diameter of that cell. From each cell's diameter, its area was computed. Density is computed by taking the inverse of the cell area. To compute the gradient in density, each 3×3 window of data points is fit to a linear equation in the x direction and to a second linear equation in the y direction. The slopes give the derivatives in the x and y directions, respectively.

Chemical treatments

Chemical treatments were blebbistatin (20 μM), U0126 (10 μM), and epidermal growth factor (EGF) (20 ng/mL). Blebbistatin and U0126 were dissolved in dimethyl sulfoxide (DMSO); EGF was dissolved in PBS. Blebbistatin and U0126 stock solutions were 20 mM and 10 mM, respectively. They were diluted by a factor of 1000 when added to the medium, leading to a DMSO concentration of 0.1% in the cell culture medium. All comparisons were made to matching concentrations of a vehicle control (DMSO or PBS).

Statistics

Statistical comparisons were made using the nonparametric Wilcoxon rank sum test in Matlab.

RESULTS

To investigate the relationship between cellular tractions and velocities, we confined monolayers of Madin-Darby canine kidney cells to circular islands (diameter 700 μm) of adhesive collagen type I. We measured cell velocities with particle image velocimetry and simultaneously measured tractions with traction force microscopy (18,21,22) (Fig. 1; Fig. S1). Similar to reports in a previous study (7), we observed sustained oscillations of inward and outward cellular motion comprising waves with a period of ~6 h (Fig. 1 b; Movie S1). To visualize the data at all points in space and time, we averaged the velocity data over the azimuthal angle to collapse all spatial data onto a single axis specifying the radial position. We then plotted the data over time to generate a kymograph. As shown in the kymograph of velocity (Fig. 1 d), the cellular motion was highly coordinated with standing waves of outward and inward collective motion, similar to seiches observed in lakes or other confined bodies of water.

Surprisingly, even though the monolayer velocity varied little with the radial position at a given time, tractions were organized in a standing wave with finite wavelength (Fig. 1 e). Although the tractions at the perimeter of the island pointed radially inward, tractions at any point within the bulk of the island oscillated radially inward and outward over time akin to the velocity field. At the perimeter of the island, all cells applied inward-pointing tractions (Fig. 1 c), indicating that these cells pulled themselves toward exterior free space, a behavior called kenotaxis (11). How-

ever, across the island, the correlation between traction and velocity was negligible (the typical correlation coefficient magnitude was $|R| < 0.1$; Fig. 1, b and c). Furthermore, the angles between the directions of velocity and traction showed a nearly uniform distribution across the monolayer (Fig. 1 f), indicating that the orientation of each cell's traction is not linked solely to its velocity.

To investigate further the relationship between traction and velocity, we considered cellular motion within an expanding cellular island wherein the cells were not restricted by a boundary. We seeded cells onto a mask with 700 μm holes placed atop a compliant polyacrylamide gel coated with collagen type I. As shown previously (4), removing this mask induces cell migration into the newly created free space. Upon sensing the free space created by mask removal, cells located at the perimeter of the island migrated first, and their outward motion caused cells just inside the perimeter to follow (Fig. S2). Over time, more and more cells began to move, creating a wave of radial motion that propagated from the perimeter to the center of the island (Fig. S2, b and d), similar to the waves of motion observed for cells in a rectangular monolayer (6). Much like the cells in the confined islands, the cells near the perimeter of the expanding islands applied inward tractions to pull themselves toward free space (Fig. S2, c and e). For cells in the bulk of the expanding island, however, we observed no alignment between directions of traction and velocity (Fig. S2 f).

These findings suggest that cells tend to apply local propulsive forces in a direction that can deviate systematically from the direction of local cellular motion. In the specific case of cells near the edge of the freely expanding monolayer, local tractions and velocities were aligned, but elsewhere they were not. Why this independence of orientations? In contrast to previous models (24,25) which predict that cells apply traction along a gradient of cellular density, our data showed no correlations between the orientations of cellular tractions, velocities, or gradients in number density (Fig. S3).

We tracked the position of each cell's nucleus to compute the average distance between each nucleus and its neighbors; from these distances, we then computed the local area covered by each cell. Within the confined islands, cellular areas increased as cells collectively moved outward and then decreased as they moved inward (Fig. 2 a). We compared the cellular areas to the stresses within the monolayer, which we measured using MSM (8,23). MSM applies the principle of force equilibrium to the cell monolayer to compute the in-plane monolayer stresses from the cell-to-substrate tractions. We found that the tension σ (defined as the mean of the two principal stresses within the cell monolayer) periodically increased and decreased with the same frequency as the radial waves in cellular velocity and with the same phase as the cellular area (Fig. 2 b), thus implying an elastic relationship. To investigate further the elastic behavior of the monolayer, we examined the relationship
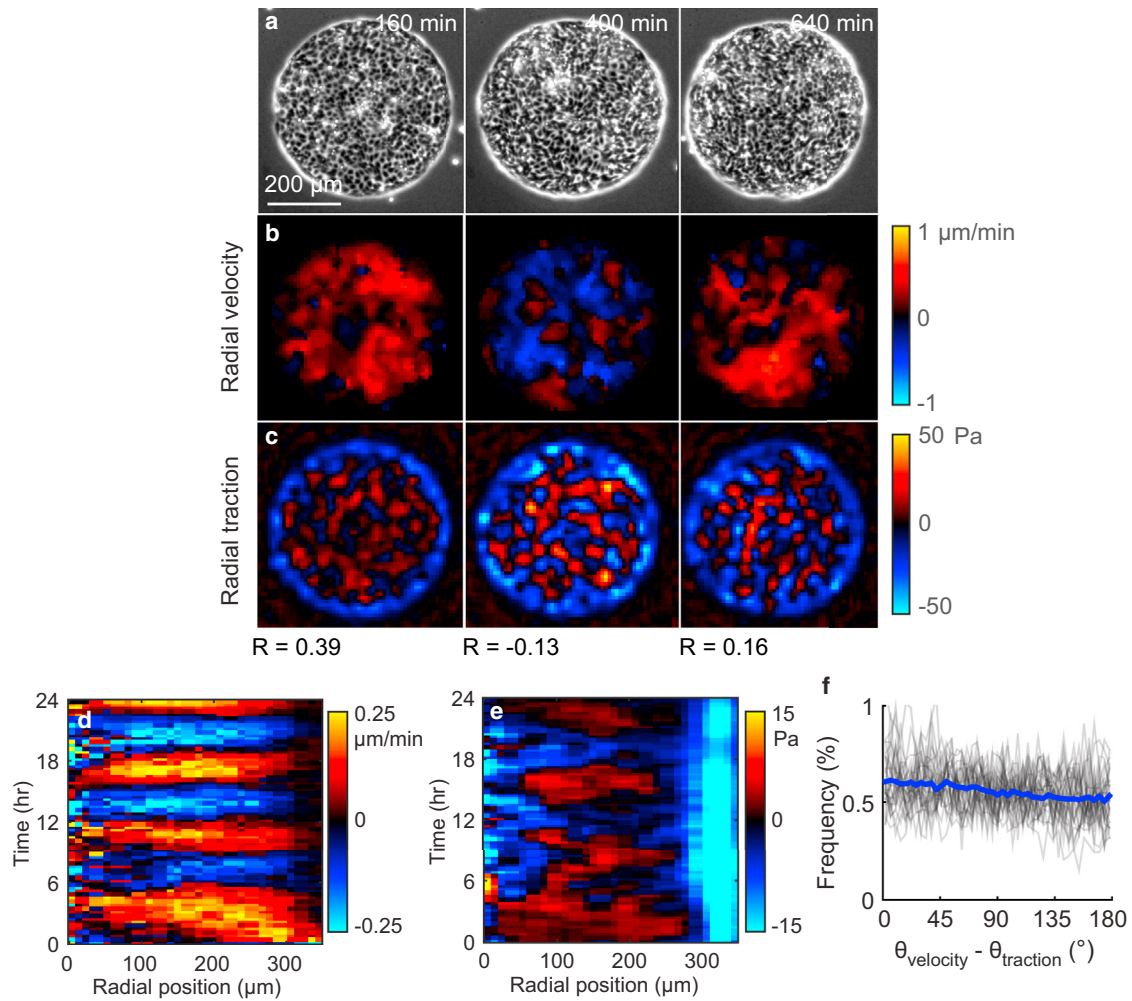
FIGURE 1 Tractions do not align with local cellular motions. (*a*) Phase-contrast images of a confined cell monolayer. Time zero corresponds to the first image collected. (*b* and *c*) The radial components of velocity (*b*) and traction (*c*) are uncorrelated with one another. At some time points (e.g., 160 min), the Pearson's correlation coefficient, *R*, is positive, and at other time points (e.g., 400 min) it is negative. (*d*) The kymograph shows the radial velocity as a function of position and time. Red and blue bands indicate oscillating outward and inward motion. (*e*) Kymograph of radial traction showing that cells at the perimeter apply tractions that point inward, whereas cells within the bulk apply tractions that oscillate between inward and outward. (*f*) Histogram of the angle between the velocity and traction vectors. Each gray line shows a single point in time for the cell island; the blue line shows all points in time. To see this figure in color, go online.

between stress and strain rate, and found no correlation (Fig. S4). The lack of correlation implied that viscous contributions to the monolayer stress are negligible. We then compared the time derivative of stress to the strain rate. Specifically, we plotted the time derivative of the tension ($d\sigma/dt$) and the trace of the strain-rate tensor ($d\varepsilon/dt$), which were well correlated over time along a single radial position (Fig. 2 *c*). The correlation is further evident by a scatter plot (Fig. 2 *d*). The elastic modulus *K* of the cell monolayer is given by the slope of a line fit to the scatter plot, $K = 113 \pm 28$ Pa (mean $\pm$ SD of $n = 8$ islands).

Similarly, cells in a freely expanding island displayed elastic behavior. As an island expanded due to outward migration, each cell within that island became stretched, thereby increasing its area (Fig. S5, *a* and *b*). Similar to the confined islands, when cells increased in area, the ten-

sion consequently increased (Fig. S5 *c*). As above, when we plotted $d\sigma/dt$ against $d\varepsilon/dt$, the data were well correlated for a single radial position (Fig. S5 *d*) and for all positions within the island (Fig. S5 *e*). For the expanding islands, we found a modulus of $K = 62 \pm 17$ Pa (mean $\pm$ SD of $n = 7$ islands). Our findings thus demonstrated that both confined and expanding cellular monolayers behave as an elastic material, albeit with different elastic moduli.

To examine the internal variables that generate cellular polarization and oscillatory waves, we developed a minimal physical model, which describes the monolayer as an elastic continuum with a displacement field $\vec{u}(\vec{r}, t)$. The assumption of elastic behavior is supported by our data and those of others (6,26) that show a linear relationship between the rate of stress and the rate of strain. As in a previously described one-dimensional model of an expanding cell
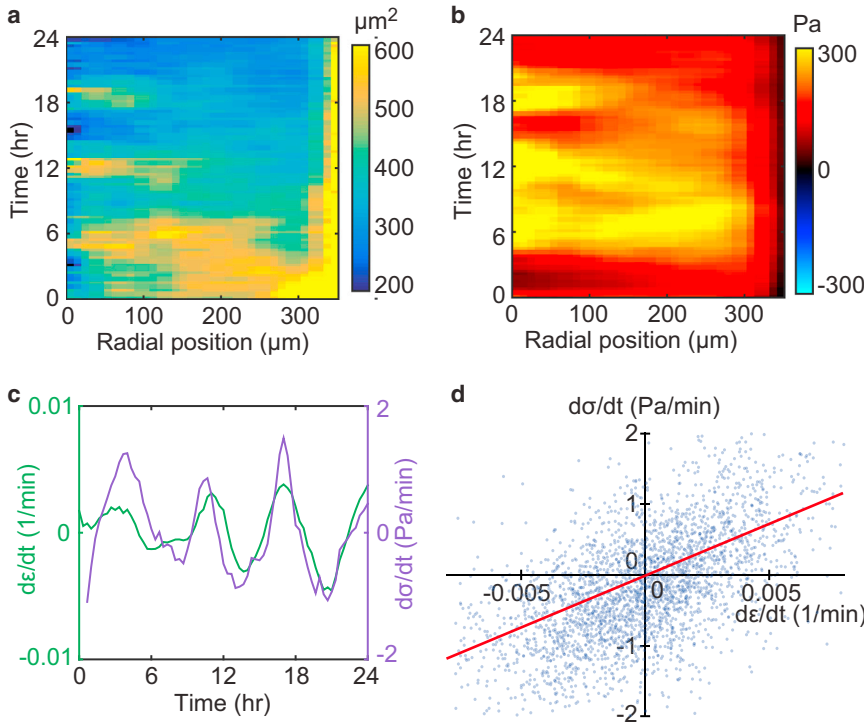
FIGURE 2 Elastic behavior of the cell monolayer. (*a*) The oscillatory motion causes expansion and contraction of each cell, shown by the oscillations in the kymograph of cell area. (*b*) Contractile tension within the monolayer oscillates in phase with the cell areas. (*c*) The area strain rate ($d\epsilon/dt$, defined as the trace of the rate-of-strain tensor) and the time derivative of tension ($d\sigma/dt$) are computed by averaging around a circle 100 μm from the center of the island and plotting over time. $d\epsilon/dt$ and $d\sigma/dt$ are well correlated (Pearson's correlation coefficient $R = 0.77$). (*d*) A scatter plot of $d\sigma/dt$ versus $d\epsilon/dt$ for all cell positions at all times shows a positive correlation ($R = 0.59$). The slope of a linear fit (*red line*) is equal to the effective elastic modulus of the monolayer, given by $K = 152$ Pa for this cell island. Experiments for $n = 8$ islands give an average value of $K = 113 \pm 28$ Pa (mean $\pm$ SD). The kymograph of velocity for this cell monolayer is shown in Fig. 1 *d*. To see this figure in color, go online.

monolayer (14), we couple this displacement field to a scalar field $c(\vec{r}, t)$ describing the concentration of a chemical signal controlling cell contractility, as elaborated below. In addition, we introduce a dimensionless vector polarization field, $\vec{p}(\vec{r}, t)$, whose magnitude describes the local degree of polarization in the cell layer. The orientation of $\vec{p}$ defines the local direction of the propulsive thrust internally generated by each cell through its adhesion to the substrate (Fig. 3 *a*) (12–15). The traction exerted by the cell layer on its substrate is therefore the difference between the viscous friction and the thrust,

$$\vec{T} = \zeta \partial_t \vec{u} - f\vec{p}, \qquad (1)$$

where ζ describes viscous friction with the substrate and f is the strength of the coupling between cell polarization and thrust (Fig. 3 *a*). The motivation for introducing the polarization field comes from our experimental data described above, which show that local cell traction is not aligned with local cell velocity, indicating that there must be an additional internal driving force in the equation of motion for the monolayer. The dynamics of the cell monolayer is overdamped and is governed by the force-balance equation,

$$h\partial_j \sigma_{ij} = T_i, \qquad (2)$$

where h is the thickness of the monolayer, and σ_{ij} is the tensor describing the in-plane stresses within the cellular monolayer, with the Latin indices representing in-plane spatial coordinates. The monolayer stress tensor σ_{ij} consists of stresses exerted by elastic and active elements within the cell and connected in parallel. As such, $\sigma_{ij} = \sigma_{ij}^{\text{el}} + \sigma_{ij}^{\text{a}}$, where σ_{ij}^{el} is the stress tensor of a linearly elastic material (27) (see the Supporting Material) and σ_{ij}^{a} is the active stress due to intracellular contractile signaling (Fig. 3 *b*). We take this to be of the form $\sigma_{ij}^{\text{a}} = \beta \log(c/c_0)\delta_{ij}$, where δ_{ij} is the Kronecker delta, and $\beta > 0$ controls the strength of the active contractile stresses. The active stress arises from a distribution of contractile force dipoles generated by myosin clusters cross-linking actin filaments in the cytoskeleton. In general, the stress contains both an isotropic term representing an active contractile tension (i.e., a negative pressure) and an anisotropic term proportional to the local polarization. Here, we neglect this anisotropic component, having verified that it does not change the behavior described below. We also neglect, for simplicity, nonlinear elasticity of the monolayer (13). The active stresses might be generated, for example, by a chemical reaction such as ATP hydrolysis, described by a concentration field, c, representing the concentration of phosphorylated myosins, with the equilibrium value given by c_0 (14). Eq. 2 is supplemented by equations governing the dynamics of the internal variables c and $\vec{p}$. The concentration of the chemical is described by a reaction-advection equation,

$$\partial_t c + \nabla \cdot (c \partial_t \vec{u}) = -\frac{1}{\tau}(c - c_0) + \alpha c_0 \nabla \cdot \vec{u}, \qquad (3)$$

where τ is the timescale of relaxation to equilibrium and $\alpha > 0$ is the rate of production of the chemical due to cellular stretching. Thus, in agreement with the experimental data
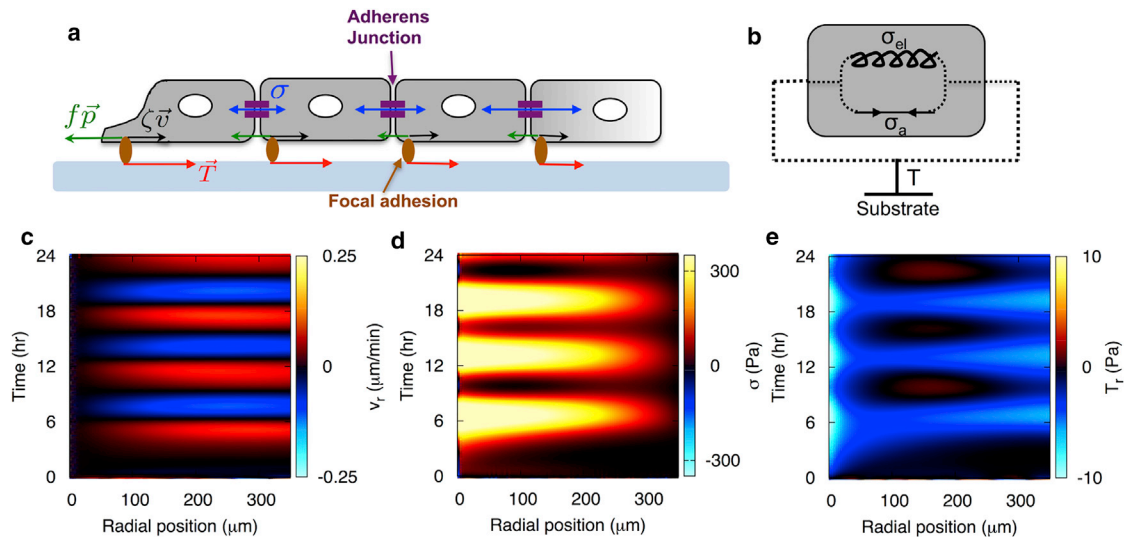
FIGURE 3 Minimal physical model capturing the wave-like motion and the distribution of traction of the cell monolayer. (*a*) Schematic of the forces acting on the cell monolayer. Tractions exerted by the monolayer on the substrate point inward (*red arrows*) at the monolayer edge and balance the forces due to viscous friction, $\zeta \boldsymbol{v}$ (*black arrows*), and propulsion, $f\vec{p}$ (*green arrows*). The monolayer is in mechanical equilibrium, such that the tractions are locally balanced by the divergence of the monolayer stress, $T_i = h\partial_j\sigma_{ij}$. (*b*) Constitutive elements of the mechanochemical model. The elastic and active elements exert stresses in parallel, and a local gradient in stress is balanced by the traction exerted by the cell on the substrate. (*c*) Kymograph of radial velocity in the cell monolayer captures the experimentally observed collective inward and outward cellular motions. (*d*) Kymograph of cellular tension in the monolayer, which increases and decreases periodically with the same frequency as the velocity. (*e*) Kymograph of radial traction. See Table S1 for a complete list of the model parameter values. To see this figure in color, go online.

(Fig. 2) and previous results for single cells (28) and multicellular monolayers (26), a local increase in cell area generates a local increase in the contractile stress $\boldsymbol{\sigma}^a$ (and vice versa). It is instructive to note that for small changes in c around its equilibrium value, Eq. 3 essentially describes the dynamics of active monolayer stress that is similar to a Maxwell constitutive model for intercellular stress proposed by Lee and Wolgemuth (12). Here, in addition, we consider an elastic contribution to the active stress, described by the term α. The dynamics of the polarization field is given by

$$\partial_t p_i = a(1 - |\vec{p}|^2)p_i + \kappa \nabla^2 p_i + w \partial_i c / c_0, \qquad (4)$$

where $\alpha > 0$ controls the rate of relaxation to a homogeneously polarized cell monolayer, and κ controls the strength of nearest-neighbor alignment of the polarization field. The active coupling $w > 0$ describes the rate of alignment of cell polarization with the gradients in the concentration field, such that local cell motion is propelled over time toward regions of high contractility. It is useful to compare our model to those of (12) and (13). The model of (13) is very similar to the one used here. Both models describe a tissue as an active elastic medium in terms of coupled equations for displacement field, polarization, and an internal scalar degree of freedom describing a deformation-induced chemical signal. Our model is a minimal version of that of (13), where many of the nonessential nonlinearities and anisotropies are ignored. In (12), in contrast, the authors describe the tissue as a fluid and retain the anisotropic part

of the active stress proportional to polarization. Internal dynamics is introduced by assuming that the stress is viscoelastic, with dynamics described by a Maxwell model. This has a similar effect to our assumption of relaxational dynamics for the chemical signal that controls the isotropic active stress. Both introduce an additional timescale that provides an effective inertia for the overdamped monolayer, be it a liquid or an elastic medium. Less direct is the comparison with the work by Basan et al. (15), who propose a particle model and assume a tendency toward alignment between cell polarization and velocity, which leads to an overall antialignment between traction and cell velocity, which does not agree with our experimental data.

By solving the coupled system given by Eqs. 2–4, assuming in-plane circular symmetry, we applied this model to the confined monolayers in our experiments (see the Supporting Material). The results are displayed in a series of kymographs showing the spatiotemporal evolution of the radial velocity, the monolayer tension, and the traction (Fig. 3, *c–e*). The model quantitatively captured multiple aspects of our experimental data, namely, that the monolayer's velocity field alternated between inward and outward motion (Fig. 3 *c*) with a time period equal to that of the oscillations in the monolayer tension (Fig. 3 *d*). This wave-like motion is predicted by the model to arise through the chemomechanical feedback between the mechanical strain and the internal state variable c (14,29). In the limiting case $c = c_0$, when the deformation $\vec{u}$ is only coupled to $\vec{p}$, no oscillatory behavior is observed (Fig. S6, *d–f*). However, if the deformation $\vec{u}$ is coupled to c only, the traction is

proportional to velocity, which contradicts our experimental observations (Fig. S6, *a–c*). This indicates that the polarization field, $\vec{p}$, is crucial to capture the misalignment between traction and velocity. Thus, coupling of the deformation $\vec{u}$ to both c and $\vec{p}$ is required to capture the experimentally observed distribution of tractions, which pointed inward at the exterior of the cell island and oscillated between outward and inward within the bulk of the island (Fig. 3 *e*).

To test the model's prediction that a feedback between mechanical strain and cellular contraction generates collective oscillations, we inhibited contraction with the myosin II inhibitor blebbistatin (20 μM). For an expanding island, blebbistatin has no effect on the speed of migration (6), but in confined islands, blebbistatin reduced each cell's speed (Fig. 4, *a* and *c*). Further, blebbistatin eliminated the multicellular oscillations (Fig. 4 *a*; Movie S2), and reduced the modulus K to ~20 Pa (Fig. 4 *d*). This observation is consistent with our model, which predicts that the coupling between strain and contractility yields an effective modulus $K \approx B + \alpha\tau(\beta + fw/2ah)$ (14), larger than the modulus B of the monolayer in the absence of contractility. Removing the coupling between strain and contractility by setting $\alpha = 0$ eliminated the oscillatory waves in our model (Fig. 4 *b*). These findings suggest that the elasticity is primarily active: the oscillations in motion cause oscillations in cellular strain, which, through active contraction, cause oscillations in tension. To further test

this, we sought to connect changes in elasticity with the motion. We found that EGF (20 ng/mL) increased the period of oscillation (Fig. 4, *e* and *g*; Movie S3). In an oscillatory system, modulus and period are inversely related, and in accord with increasing the period, treatment with EGF decreased the modulus K (Fig. 4 *h*). When we reduced the magnitude of the constants that couple tension and strain, α and β, we saw, similarly, an increase in the period of oscillations (Fig. 4 *f*). From these findings—that the waves require contraction and that the period depends inversely on modulus—we conclude that the elasticity is not passive in nature; rather, it is the result of myosin-driven contractility within the cell.

DISCUSSION

Here, we have studied motions and forces in a confined monolayer of epithelial cells. Spontaneous oscillations arise wherein cells alternate between outward and inward correlated motions that resemble the sloshing seiches that are observed in confined bodies of water. The direction of local cellular velocity is generally independent of the direction of local traction, thus indicating that the relationship between force and motion requires additional state variables. Two cellular state variables, the concentration of contractile elements and the polarization of cell motion, were introduced
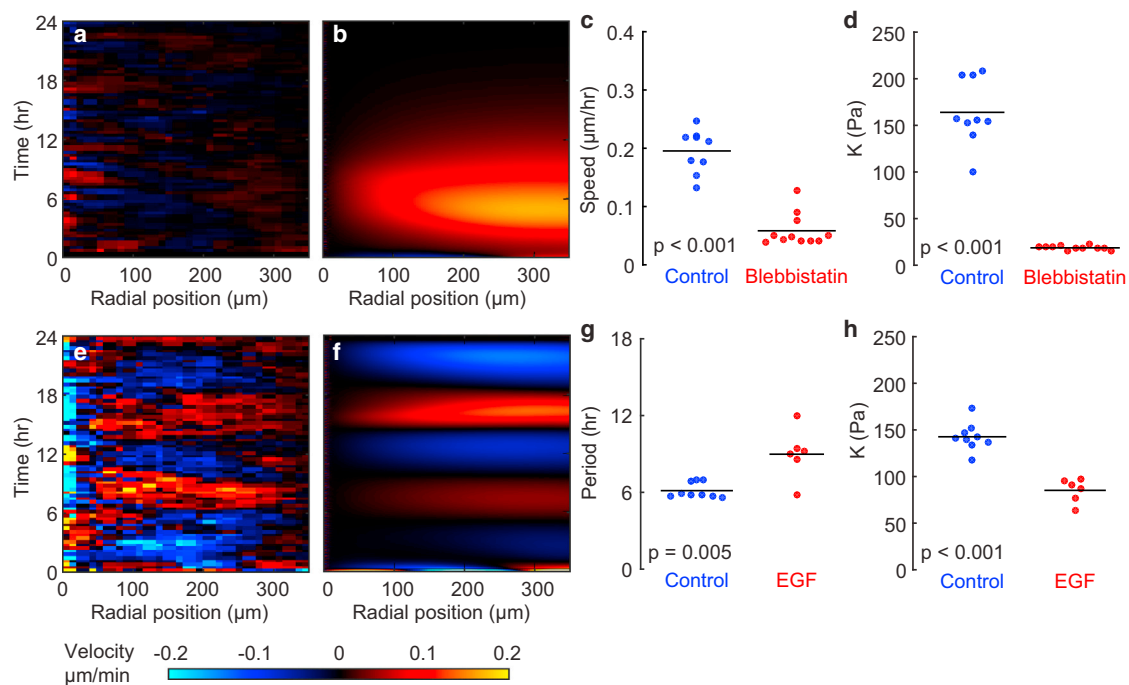
FIGURE 4 The waves of collective motion and elasticity in the monolayer depend on the contractile activity of the cells. (*a*) Kymograph of radial velocity after treatment with blebbistatin shows reduction in speed and elimination of oscillatory waves of radial motion. (*b*) Simulated kymograph of radial velocity using the model with no feedback between strain and contractility ($\alpha = 0$) also shows elimination of waves. (*c* and *d*) Treatment with blebbistatin reduces root mean-square speed of cells by a factor of ~4 (*c*) and reduces the modulus K to a nearly negligible value (*d*). (*e*) Kymograph of radial velocity for an island treated with EGF (20 ng/mL). (*f*) Simulated kymograph with reduced values of the parameters α and β. (*g*) Compared with the control, EGF increased the period of oscillation. (*h*) Relative to the control, treatment with EGF decreased the effective elastic modulus, K. For the plots in (*c*), (*d*), (*g*), and (*h*), each dot corresponds to a different cell island. *p*-values are computed using a rank-sum statistical test. To see this figure in color, go online.

to reproduce the experimental results. The coupling between the cellular strain and chemical concentration generates effective inertia, which, together with cellular elasticity, supports the oscillatory waves of motion observed in the experiments. Decreasing the elastic modulus with EGF increased the period of oscillation (Fig. 4, g and h), in agreement with the theory.

Elasticity of the monolayer has been previously attributed to a passive spring-like behavior of the cytoskeleton, its contractile apparatus, and cell-cell adhesions (6,7). In contrast, our model now incorporates a feedback between cellular strain and contractility such that a local increase in cell area induces larger contractility. This mechanism is consistent with recent experiments on single cells (28) and multicellular clusters (26,30), which show that cells with larger area are more contractile than cells with smaller area. When we suppressed cell contractility with the myosin-II inhibitor blebbistatin, the elastic modulus decreased by an order of magnitude (Fig. 4 d), and the waves were suppressed (Fig. 4 a). From this observation we conclude that the elasticity required to generate the waves is not simply a passive spring-like behavior; rather, it results from the active contractile elements inside the cell (26). Adding blebbistatin reduced the average cell speed in these confined islands, but such a reduction in speed is unlikely to be the mechanism that inhibits the oscillations in cellular motion. A previous study showed that blebbistatin in an expanding cellular island has no effect on cell speed, but it does eliminate propagating waves of contractile tension (6). This observation agrees with our finding that active cell contraction is required to generate the oscillatory waves.

The molecular mechanisms that link changes in cellular stretching to changes in contractile tension are unknown, but theoretical studies (13) and experimental evidence point to ERK MAP kinase (ERK1/2) as being associated with extension of muscle tissue (31) and stretching of stress fibers (32). Moreover, when a monolayer begins to expand into free space, a wave of ERK1/2 phosphorylation propagates from the monolayer's free edge into the bulk (33,34) at a speed approximately the same as that of the waves of cellular motion that occur in our experiments of expanding cellular islands (Fig. S2 d) and have been reported elsewhere (6). This slow-moving wave results not from damage to the monolayer, but rather from the free space offered to the monolayer's edge (34). When we inhibited ERK1/2 with U0126 (10 μM), the effective modulus decreased by a factor of 2, and collective oscillations were suppressed (Fig. S7; Movie S4).

Collective cellular oscillations similar to the ones described here have been reported by Deforet et al. (7), who performed stochastic particle-based simulations that balanced the forces of inertia, friction, intercellular adhesions, and active propulsion. In their simulation, each cell was given a tendency to adapt its velocity to that of its nearest neighbors. Although the model by Deforet et al. and the one presented here are both based on local force-balance, they differ in spirit. Instead of simulating the dynamics of individual cells, we propose a continuum model formulated in terms of a few coarse-grained fields such as traction and velocity, which are measured directly in the experiments. Our model contains only a small number of parameters that represent effective material properties of the monolayer and describe the combined effect of a number of signaling pathways. The model makes testable predictions that provide a way of correlating the macroscopic parameters of the theory with specific pathways.

Oscillatory or wavelike motion requires second-order differential equations in time, corresponding to the tradeoff between two independent timescales. The dynamics of cellular monolayers is overdamped, hence governed by a first-order differential equation, with a single timescale determined by the interplay of viscous friction and elasticity. Until now, the origin of the second timescale required for oscillatory behavior has remained mysterious. Deforet et al. accounted for the second timescale by introducing cellular inertia (7). Serra-Picamal et al. accounted for the second timescale by assuming that stretched cells became fluidized (i.e., they flowed under tensile forces) for a specified period of time (6). There is evidence that cells fluidize when stretched and unstretched quickly (35–37), but whether stretches due to slow cellular motion induce fluidization remains an open question. Our model and experiments point to a second timescale that comes from the mechanochemical feedback (13) between the local strain and the rate of change in contractile tension. This feedback mechanism results in self-sustained periods of stiffening and fluidization in the cell monolayer (14).

Dynamics of the chemical concentration c does not explain the apparent independence between the local orientations of traction and velocity (Fig. 1 f; Figs. S2 f and S8). Whereas Kim et al. showed that velocity and tractions do not align near a boundary (11), we show here that an angle of misalignment between traction and velocity occurs even in the absence of a boundary. The histogram of the angle between traction and velocity at all points in time (Fig. 1 f, blue line) shows a very small peak near zero, indicating a slight tendency for cells to pull on the substrate in the same direction that they move. This occasional alignment between motion and traction is consistent with the presence of a viscous drag exerted by the moving cells onto the substrate, as described by our model and those of others (12–15). In these models, the viscous-drag term connects tractions to motion, and thus, our observation of occasional alignment between traction and velocity serves as a confirmation of this connection.

To account for the deviation between the local directions of traction and velocity, we propose a vector polarization field that locally directs the cellular motion. Other theoretical models have also incorporated a cell polarization field defining the orientation of an anisotropic dipole-like contractile stress (12), with dynamics governed by general

nonlinear hydrodynamic equations of polar liquid crystals (13,38). In contrast, our work considers a *minimal* model where cell polarization does not generate shear stresses, in agreement with our experimental data that show an isotropic distribution of the monolayer stress field (Fig. S9). Importantly, we identify two physical mechanisms that control the dynamics of cell polarization. First, cells tend to polarize their traction toward free space, consistent with kenotaxis (11). Our model accounts for kenotaxis in the first term on the righthand side of Eq. 4, which tends to polarize the monolayer toward free space. Second, the polarization field evolves in time so as to locally align toward regions of high contractile tension in the monolayer (Fig. S10). These two tendencies are required to reproduce the spatial patterning of the traction field (Figs. 1 *e* and 3 *e*), and they provoke the question of what molecular mechanism generates the polarization. The cytoskeletal protein merlin may be involved, as the feedback between merlin and Rac1 has been shown to direct formation of lamellipodia in collective cellular migration (9). If merlin indeed polarizes the cells, it is likely only one of several molecular mechanisms controlling the forces that drive collective cellular motion.

Here, we have found that the various biological mechanisms controlling the waves of collective motion combine together to relate force and motion through two physical variables, one controlling intracellular contractility and the other controlling polarized cell motion. These two state variables are present within each cell, but perhaps even more striking is the fact that each cell coordinates these state variables with its neighbors to generate emergent waves of correlated motion that span multiple cell diameters. Emergent phenomena like these multicellular waves control the motion and final positioning of the cellular collective, and thus, they are likely to play a key role in development and disease. The two internal variables that we describe here—cell contraction and polarization—provide a framework for further investigation.

SUPPORTING MATERIAL

Supporting Materials and Methods, eleven figures, one table, and four movies are available at http://www.biophysj.org/biophysj/supplemental/S0006-3495(16)30301-0.

AUTHOR CONTRIBUTIONS

J.N., S.B., M.C.M., J.B., and J.J.F designed the research. J.N. performed the experiments. S.B. and K.J.C.U. performed the simulations. B.G., H.J., Y.P., and J.S. developed experimental protocols. J.N., S.B., K.J.C.U., B.G. M.C.M., J.B., and J.J.F. discussed the results. J.N., S.B., M.C.M., and J.J.F wrote the manuscript.

ACKNOWLEDGMENTS

We thank Adrian Pegoraro for providing the cells.

REFERENCES

1. Friedl, P., and K. Wolf. 2003. Tumour-cell invasion and migration: diversity and escape mechanisms. *Nat. Rev. Cancer.* 3:362–374.

2. Martin, P., and S. M. Parkhurst. 2004. Parallels between tissue repair and embryo morphogenesis. *Development.* 131:3021–3034.

3. Friedl, P., and D. Gilmour. 2009. Collective cell migration in morphogenesis, regeneration and cancer. *Nat. Rev. Mol. Cell Biol.* 10:445–457.

4. Poujade, M., E. Grasland-Mongrain, …, P. Silberzan. 2007. Collective migration of an epithelial monolayer in response to a model wound. *Proc. Natl. Acad. Sci. USA.* 104:15988–15993.

5. Angelini, T. E., E. Hannezo, …, D. A. Weitz. 2011. Glass-like dynamics of collective cell migration. *Proc. Natl. Acad. Sci. USA.* 108:4714–4719.

6. Serra-Picamal, X., V. Conte, …, X. Trepat. 2012. Mechanical waves during tissue expansion. *Nat. Phys.* 8:628–634.

7. Deforet, M., V. Hakim, …, P. Silberzan. 2014. Emergence of collective modes and tri-dimensional structures from epithelial confinement. *Nat. Commun.* 5:3747.

8. Tambe, D. T., C. C. Hardin, …, X. Trepat. 2011. Collective cell guidance by cooperative intercellular forces. *Nat. Mater.* 10:469–475.

9. Das, T., K. Safferling, …, J. P. Spatz. 2015. A molecular mechanotransduction pathway regulates collective migration of epithelial cells. *Nat. Cell Biol.* 17:276–287.

10. Zaritsky, A., E. S. Welf, …, G. Danuser. 2015. Seeds of locally aligned motion and stress coordinate a collective cell migration. *Biophys. J.* 109:2492–2500.

11. Kim, J. H., X. Serra-Picamal, …, J. J. Fredberg. 2013. Propulsion and navigation within the advancing monolayer sheet. *Nat. Mater.* 12:856–863.

12. Lee, P., and C. W. Wolgemuth. 2011. Crawling cells can close wounds without purse strings or signaling. *PLOS Comput. Biol.* 7:e1002007.

13. Köpf, M. H., and L. M. Pismen. 2013. A continuum model of epithelial spreading. *Soft Matter.* 9:3727–3734.

14. Banerjee, S., K. J. C. Utuje, and M. C. Marchetti. 2015. Propagating stress waves during epithelial expansion. *Phys. Rev. Lett.* 114:228101.

15. Basan, M., J. Elgeti, …, H. Levine. 2013. Alignment of cellular motility forces with tissue flow as a mechanism for efficient wound healing. *Proc. Natl. Acad. Sci. USA.* 110:2452–2459.

16. Kabla, A. J. 2012. Collective cell migration: leadership, invasion and segregation. *J. R. Soc. Interface.* 9:3268–3278.

17. Zimmermann, J., R. L. Hayes, …, H. Levine. 2014. Intercellular stress reconstitution from traction force data. *Biophys. J.* 107:548–554.

18. Trepat, X., M. R. Wasserman, …, J. J. Fredberg. 2009. Physical forces during collective cell migration. *Nat. Phys.* 5:426–430.

19. Schindelin, J., I. Arganda-Carreras, …, A. Cardona. 2012. Fiji: an open-source platform for biological-image analysis. *Nat. Methods.* 9:676–682.

20. Treloar, K. K., and M. J. Simpson. 2013. Sensitivity of edge detection methods for quantifying cell migration assays. *PLoS One.* 8:e67389.

21. Butler, J. P., I. M. Tolic-Norrelykke, …, J. J. Fredberg. 2002. Traction fields, moments, and strain energy that cells exert on their surroundings. *Am. J. Physiol. Cell Physiol.* 282:C595–C605.

22. Del Alamo, J. C., R. Meili, …, J. C. Lasheras. 2007. Spatio-temporal analysis of eukaryotic cell motility by improved force cytometry. *Proc. Natl. Acad. Sci. USA.* 104:13343–13348.

23. Tambe, D. T., U. Croutelle, …, J. J. Fredberg. 2013. Monolayer stress microscopy: limitations, artifacts, and accuracy of recovered intercellular stresses. *PLoS One.* 8:e55172.

24. Arciero, J. C., Q. Mi, …, D. Swigon. 2011. Continuum model of collective cell migration in wound healing and colony expansion. *Biophys. J.* 100:535–543.

25. Li, B., and S. X. Sun. 2014. Coherent motions in confluent cell monolayer sheets. *Biophys. J.* 107:1532–1541.

26. Vincent, R., E. Bazellières, …, X. Trepat. 2015. Active tensile modulus of an epithelial monolayer. *Phys. Rev. Lett.* 115:248103.

27. Landau, L. D., and E. M. Lifshitz. 1986. Course of Theoretical Physics: Theory of Elasticity. Butterworth Heinemann, Oxford, United Kingdom.

28. Oakes, P. W., S. Banerjee, …, M. L. Gardel. 2014. Geometry regulates traction stresses in adherent cells. *Biophys. J.* 107:825–833.

29. Dierkes, K., A. Sumi, …, G. Salbreux. 2014. Spontaneous oscillations of elastic contractile materials with turnover. *Phys. Rev. Lett.* 113:148102.

30. Mertz, A. F., S. Banerjee, …, E. R. Dufresne. 2012. Scaling of traction forces with the size of cohesive cell colonies. *Phys. Rev. Lett.* 108:198101.

31. Martineau, L. C., and P. F. Gardiner. 2001. Insight into skeletal muscle mechanotransduction: MAPK activation is quantitatively related to tension. *J. Appl. Physiol.* 91:693–702.

32. Hsu, H. J., C. F. Lee, …, R. Kaunas. 2010. Stretch-induced stress fiber remodeling and the activations of JNK and ERK depend on mechanical strain rate, but not FAK. *PLoS One.* 5:e12470.

33. Matsubayashi, Y., M. Ebisuya, …, E. Nishida. 2004. ERK activation propagates in epithelial cell sheets and regulates their migration during wound healing. *Curr. Biol.* 14:731–735.

34. Nikolić, D. L., A. N. Boettiger, …, S. Y. Shvartsman. 2006. Role of boundary conditions in an experimental model of epithelial wound healing. *Am. J. Physiol. Cell Physiol.* 291:C68–C75.

35. Trepat, X., L. Deng, …, J. J. Fredberg. 2007. Universal physical responses to stretch in the living cell. *Nature.* 447:592–595.

36. Krishnan, R., C. Y. Park, …, J. J. Fredberg. 2009. Reinforcement versus fluidization in cytoskeletal mechanoresponsiveness. *PLoS One.* 4:e5486.

37. Krishnan, R., E. P. Canovic, …, D. Stamenovic. 2012. Fluidization, resolidification, and reorientation of the endothelial cell in response to slow tidal stretches. *Am. J. Physiol. Cell Physiol.* 303:C368–C375.

38. de Gennes, P. G., and J. Prost. 1995. The Physics of Liquid Crystals. Clarendon Press, Oxford, United Kingdom.

Supplemental Information

Cellular Contraction and Polarization Drive Collective Cellular Motion

Jacob Notbohm, Shiladitya Banerjee, Kazage J.C. Utuje, Bomi Gweon, Hwanseok Jang, Yongdoo Park, Jennifer Shin, James P. Butler, Jeffrey J. Fredberg, and M. Cristina Marchetti

Monolayer stress microscopy

Here we detail our experimental technique for recovering intercellular stresses from tractions, called mono-layer stress microscopy (MSM; Refs. 8, 23). The concept underlying monolayer stress microscopy is force equilibrium applied to the cell layer. Assuming the layer to be thin with no variation through the thickness, the two equilibrium equations are

$$\frac{\partial \sigma_{xx}}{\partial x} + \frac{\partial \sigma_{xy}}{\partial y} + \frac{T_x}{h} = 0$$
$$\frac{\partial \sigma_{xy}}{\partial x} + \frac{\partial \sigma_{yy}}{\partial y} + \frac{T_y}{h} = 0,$$
(1)

where σ_{ij} are components of the in-plane stress tensor, T_i is the i-th component of the traction vector applied by the substrate to the monolayer, and h is the thickness of the monolayer. These equations are independent of the constitutive properties of the monolayer; they result directly from a balance of forces. Note that in one dimension (chosen in the x direction) Eqs. (1) would reduce to the single equation

$$\frac{\partial \sigma_{xx}}{\partial x} + \frac{T_x}{h} = 0 ,$$
(2)

which can immediately be integrated to obtain the cellular stress σ_{xx} with no assumption on the form of the constitutive equation.

In two dimensions, however, the stress tensor has three unique components, so a third equation is required. In the original implementation of MSM (8, 23), the monolayer was assumed to behave as a linear elastic material, giving the following two-dimensional (2D) constitutive relationship between stress and strain:

$$\sigma_{ij} = \frac{E\nu}{1-\nu^2} \varepsilon_{kk}\delta_{ij} + \frac{E}{1+\nu}\varepsilon_{ij},$$
(3)

where E is Young's modulus, ν is Poisson's ratio, and ε_{ij} are components of the in-plane strain tensor. Here summation over repeated indices is implied. Assuming the monolayer is homogeneous, the constitutive equation combined with Eqs. 1 and compatibility of strain (requiring that the strain be the derivative of a unique vector field),

$$\frac{\partial^2 \varepsilon_{xx}}{\partial y^2} + \frac{\partial^2 \varepsilon_{yy}}{\partial x^2} = 2\frac{\partial^2 \varepsilon_{xy}}{\partial x \partial y},$$
(4)

give the Beltrami–Michell equation (23),

$$\nabla^2 (\sigma_{xx} + \sigma_{yy}) = -\frac{1+\nu}{h} \left(\frac{\partial T_x}{\partial x} + \frac{\partial T_y}{\partial y} \right).$$
(5)

Together, Eqs. 1 and 5 can be solved for the three independent components of the stress tensor σ_{ij}. Note that the equations are independent of Young's modulus; furthermore it has been shown that dependence on Poisson's ratio is sufficiently weak to make it negligible (23).

We now discuss the case where the cell layer is a linear viscous material. In this case the 2D constitutive equation is

$$\sigma_{ij} = -p\delta_{ij} + (\mu_b - \mu_s)\dot{\varepsilon}_{kk}\delta_{ij} + 2\mu_s\dot{\varepsilon}_{ij},$$
(6)

where p is the thermodynamic pressure, μ_b and μ_s are the bulk and shear viscosities, respectively, and the overdot represents a partial derivative in time. Requiring that the strain rate $\dot{\varepsilon}_{ij}$ be the derivative of a unique vector field (the local velocity) yields a compatibility equation

$$\frac{\partial^2 \dot{\varepsilon}_{xx}}{\partial y^2} + \frac{\partial^2 \dot{\varepsilon}_{yy}}{\partial x^2} = 2\frac{\partial^2 \dot{\varepsilon}_{xy}}{\partial x \partial y}.$$
(7)

2

If we assume the layer to be incompressible and neglect pressure gradients, we can combine Eqs. 1, 6, and 7 to obtain

$$\nabla^2 \left(\sigma_{xx} + \sigma_{yy} \right) = -\frac{\left(\frac{2\mu_b}{\mu_b + \mu_s} \right)}{h} \left(\frac{\partial T_x}{\partial x} + \frac{\partial T_y}{\partial y} \right),$$ (8)

which is equivalent to Eq. 5. In this case the conventional method used to infer stress from traction in MSM applies regardless of whether a material is elastic or viscous. In general, however, in a fluid density fluctuations are not slaved to strain fluctuations and an additional condition is needed to determine the pressure. Whether such a pressure exists in a cell monolayer remains unknown.

Recent work by Zimmermann et al. (17) has provided independent validation of the method used in MSM. In their verification, Zimmermann et al. simulated collective cell motion using a particle-based model. The particles in the model represented cells, and were able to flow freely past one another with no memory of their previous position, therefore behaving like a fluid where particles do not maintain the same neighbors in the course of time. Zimmermann et al. then computed the stresses directly from the simulations and compared them to stresses computed with MSM. The comparison showed close agreement (17), suggesting that MSM can be applied to either an elastic or a viscous material, and that pressure variations do not play an important role in the viscous case.

Minimal physical model of collective cell motion

Continuum model. Here we provide a detailed description of the minimal physical model introduced in the main text. We consider a thin film of cell monolayer confined to a circular micro-pattern of radius R with average height h. We describe the monolayer as an elastic continuum whose vector displacement at position $\mathbf{r}$ and at time t is given by $\mathbf{u}(\mathbf{r},t)$. The local displacements of the monolayer are coupled to two internal degrees of freedom, the concentration $c(\mathbf{r},t)$ of a regulatory chemical controlling cell contractility, and a dimensionless vector field $\mathbf{p}(\mathbf{r},t)$ controlling the angle of misalignment between local cell motion and propulsive traction forces. The magnitude of $\mathbf{p}$ accounts for the amount of misalignment between cell motion and traction, whereas its orientation defines the direction of the thrust force acting on the cell. In the absence of external forces, in-plane force balance gives,

$$\partial_j \Sigma_{ij} + \partial_z \Sigma_{iz} = 0 \,,$$ (9)

where Σ is the stress tensor of the monolayer and latin indices denote in-plane coordinates x and y. For $h \ll R$, we average the force balance across the z-direction, assuming that the top surface of the monolayer at $z = h$ is stress free, i.e. $\Sigma_{iz}|_{z=h} = 0$. This gives us,

$$h\partial_j \sigma_{ij} = \Sigma_{iz}|_{z=0},$$ (10)

where $\sigma_{ij}(x,y) = h^{-1} \int_0^h dz \, \Sigma_{ij}(x,y,z)$ is the thickness averaged stress tensor of the monolayer equivalent to what is measured in experiments. We identify the shear stress at the cell–substrate interface, $\Sigma_{iz}|_{z=h}$, as the traction stress T_i exerted by the cell on the substrate. This gives us the following relation between monolayer stress and traction,

$$T_i = h\partial_j \sigma_{ij},$$ (11)

The monolayer stress tensor is given by the sum of passive elastic and active elements connected in parallel (Fig. 3b), $\sigma_{ij} = \sigma_{ij}^{\text{el}} + \sigma_{ij}^{\text{a}}$, where the passive elastic component of the stress tensor, σ_{ij}^{el}, is assumed to be isotropic and homogeneous. It is given by,

$$\sigma_{ij}^{\text{el}} = B\varepsilon_{kk}\delta_{ij} + 2G \left(\varepsilon_{ij} - \frac{1}{2}\delta_{ij}\varepsilon_{kk} \right) \,.$$ (12)

3

B and G are respectively the in-plane bulk and shear elastic moduli of the monolayer, ε_{ij} the symmetrized strain tensor, $\varepsilon_{ij} = \frac{1}{2}(\partial_i u_j + \partial_j u_i)$ and δ_{ij} the Kronecker delta. The active stress σ_{ij}^{a} is taken to be proportional to the logarithm of the concentration field, $\log(c/c_0)$, where c_0 is the concentration at chemical equilibrium when no stress is generated. Although we are not aware of any direct measurement of active stress in live cells and their relationships with myosin concentration and chemical potential of ATP, the logarithmic dependence of active stress on concentration follows from two simple assumptions. First, we assume the presence of weak to moderate activity level in cells such that the stress depends linearly on the chemical potential. Second, the chemical potential difference is related logarithmically the concentration of reactants and products given the partial pressure of the molecules are linearly dependent on the concentration. We thus have,

$$\sigma_{ij}^{\mathrm{a}} = \beta \log(c/c_0)\delta_{ij} \,, \tag{13}$$

where $\beta > 0$ is the magnitude of the active contractile stresses generated by molecular motors and c_0 is the equilibrium concentration. The assumption of isotropic stress is consistent with the stress field measured in our experiments using monolayer stress microscopy. Our principal stress analysis reveals that the stress ellipses in the monolayer typically have low aspect ratio with a quotient of maximum shear to tension less than 0.2 (Supporting Fig. S9). The dynamics of the displacement field, $\mathbf{u}(\mathbf{r},t)$, is given by

$$\zeta \partial_t u_i = f p_i + h \partial_j \sigma_{ij} \tag{14}$$

where ζ describes viscous friction with the substrate and the constant f is the magnitude of the coupling between polarization and motion and quantifies the strength of the propulsion force. The resultant traction applied by the cells on the substrate is thus, $\mathbf{T} = \zeta \partial_t \mathbf{u} - f\mathbf{p}$. The dynamics of the concentration field $c(\mathbf{r},t)$ is given by,

$$\partial_t c + \boldsymbol{\nabla} \cdot (c\partial_t \mathbf{u}) = -\frac{1}{\tau}(c - c_0) + \alpha c_0 \varepsilon_{kk} \,, \tag{15}$$

where τ is the timescale of actomyosin relaxation to equilibrium and α is the rate of production of c due to cellular stretching. The second term on the left hand side of Eq. (15) describes convection of chemicals by local cell motion. The dynamics of the polarization field $\mathbf{p}(\mathbf{r},t)$ is given by,

$$\partial_t p_i = a\left(1 - |\mathbf{p}|^2\right)p_i + \kappa \nabla^2 p_i + w\partial_i(c/c_0) \,, \tag{16}$$

where the first two terms allow for the onset of a homogeneously polarized system, $|\mathbf{p}| = 1$, and $a\,(>0)$ is the rate of relaxation to the homogeneous state $|\mathbf{p}| = 1$. Local cost of fluctuations in polarization is characterized by an isotropic stiffness κ with dimensions of diffusivity; it describes the tendency of cell polarization to align with its neighbors. The active coupling w describes the local rate of alignment of cell polarization with the gradients of the concentration field.

Numerical solution in circular geometry. We numerically solve the model equations in a circular geometry by assuming in-plane rotational symmetry such that all quantities depend solely on the radial coordinate, r. Rotational symmetry in polar coordinates implies that shear stresses $\sigma_{r\theta}$ vanish and the dynamics of the radial displacement field are solely governed by normal stresses, in agreement with the experiments (Supporting Fig. S9). The equation of motion for radial displacements u_r is given by,

$$\zeta \partial_t u_r = f p_r + h\left(\partial_r \sigma_{rr} + \frac{1}{r}(\sigma_{rr} - \sigma_{\theta\theta})\right) \,, \tag{17}$$

where σ_{rr} and $\sigma_{\theta\theta}$ define the radial and orthoradial components of the normal stress in the monolayer, given by,

$$\sigma_{rr} = B\left(\partial_r u_r + \frac{u_r}{r}\right) + G\left(\partial_r u_r - \frac{u_r}{r}\right) + \beta\log(c/c_0)\,, \tag{18}$$

$$\sigma_{\theta\theta} = B\left(\partial_r u_r + \frac{u_r}{r}\right) - G\left(\partial_r u_r - \frac{u_r}{r}\right) + \beta\log(c/c_0)\,. \tag{19}$$

The equation governing the dynamics of c is given by,

$$\partial_t c + \frac{1}{r}\partial_r\left(rc\partial_t u_r\right) = -\frac{1}{\tau}(c - c_0) + \alpha c_0\left(\partial_r u_r + \frac{u_r}{r}\right)\,. \tag{20}$$

Finally, the equation governing the dynamics of radial polarization, p_r, is given by

$$\partial_t p_r = a\left(1 - p_r^2\right)p_r + \frac{\kappa}{r}\partial_r(r\partial_r p_r) + w\partial_r(c/c_0)\,. \tag{21}$$

The homogeneous solutions to the above equation, $p_r = \pm 1$, describe uniformly polarized states of the cell monolayer with the cell motion pointing radially outwards for $p_r = 1$ and inward for $p_r = -1$. The solution $p_r = 1$ describes the tendency of cell motion to polarize towards the free space at the exterior of the cell island, consistent with *kenotaxis* (10).

To solve the above equations, we assume that no external forces act at the outer boundary such that $\sigma_{ij}n_j = 0$ where n_j is the outward unit normal vector to the boundary. This translates to the boundary condition $\sigma_{rr}(R) = 0$ in circular geometry. We model adhesion with the micropattern by anchoring a hookean spring of stiffness 0.03 Pa/μm at the boundary of the cell monolayer. We choose a no-flux boundary condition for c and p_r, such that $\partial_r c(R) = 0$, and the gradients of the polarization variable at the outer boundary is zero, $\partial_r p_r(R) = 0$. We also assume that the monolayer is initially undeformed, $u(r,0) = 0$, and unpolarized, $p_r(r,0) = 0$, with an equilibrium concentration of contractile elements, $c(r,0) = c_0$. We then integrate numerically Eqs. (17), (20) and (21) with the given initial and boundary conditions by means of the Runge–Kutta–Fehlberg method. We solve three different implementations of the model:

- **u-p** *model.* Radial displacement u_r is coupled only to p_r and the concentration field is assumed to be constant, $c = c_0$. In this case no wave-like behavior is obtained (Supporting Fig. S6 d–f), indicating that the mechanochemical coupling between c and u_r is crucial to reproduce the waves of oscillatory motion.

- **u-c** *model.* Displacement u_r is coupled to c only. The polarization field and hence the propulsion force fp_r are set to zero. In this case we obtain standing waves qualitatively similar to those seen in experiments (Supporting Fig. S6 a–c). However, the traction is proportional to velocity, in contrast to the misalignment observed in experiments.

- **u-c-p** *model.* Here we use the full equations of motion, coupling u_r to both c and p_r and are able to quanitatively reproduce the experimental trends (Fig. 3).

Finite difference spatial discretization scheme. To solve Eqs. (17), (20) and (21) numerically, we first spatially discretize the equations using the central finite difference method and then integrate them numerically by means of the Runge–Kutta–Fehlberg method. At every time step, the spatial domain spans from 0 to

R, where R is the radius of the cell monolayer. The numerical approximation to the functions $u_r(r,t)$, $c(r,t)$ and $p_r(r,t)$ at the spatial grid point $r_i = i\Delta r$ with $\Delta r = R/(N-1)$ and $i = 1, N-2$, are denoted as $u_n^i(t_n)$, $c_n^i(t_n)$ and $p_n^i(t_n)$ respectively. In the following, we drop the argument t_n of the functions for convenience. Substituting Eqs. (18) and (19) in Eq. (17), the equation of motion is spatially discretized as follows,

$$\zeta \partial_t u_n^i = f p_n^i + h \left[(B+G) \left(\left(\frac{u_n^{i+1} + u_n^{i-1} - 2u_n^i}{\Delta r^2} \right) + \left(\frac{u_n^{i+1} - u_n^{i-1}}{2 r_i \Delta r} \right) - \frac{u_n^i}{r_i^2} \right) + \beta \left(\frac{c_n^{i+1} - c_n^{i-1}}{2 c_n^i \Delta r} \right) \right] . \quad (22)$$

The spatial discretization of Eq. (20) gives,

$$\partial_t c_n^i + \frac{1}{r_i} \left(c_n^i \partial_t u_n^i \right) + \left(\frac{c_n^{i+1} - c_n^{i-1}}{2\Delta r} \right) \partial_t u_n^i + c_n^i \left(\frac{\partial_t u_n^{i+1} - \partial_t u_n^{i-1}}{2\Delta r} \right) = -\frac{1}{\tau} \left(c_n^i - c_0 \right) + \alpha c_0 \left(\frac{u_n^{i+1} - u_n^{i-1}}{2\Delta r} + \frac{u_n^i}{r_i} \right) . \quad (23)$$

The spatial discretization of Eq. (21) gives,

$$\partial_t p_n^i = a \left(1 - (p_n^i)^2 \right) p_n^i + \kappa \left(\frac{p_n^{i+1} + p_n^{i-1} - 2p_n^i}{\Delta r^2} \right) + \kappa \left(\frac{p_n^{i+1} - p_n^{i-1}}{2 r_i \Delta r} \right) + w \left(\frac{c_n^{i+1} - c_n^{i-1}}{2 c_0 \Delta r} \right) . \quad (24)$$

At $i = 0$, the boundary conditions for the above discretized equations are given by: $\zeta \partial_t u_n^0 = 0$, $\partial_t c_n^0 = -\frac{1}{\tau} \left(c_n^0 - c_0 \right)$ and $\partial_t p_n^0 = a \left(1 - (p_n^0)^2 \right) p_n^0 + 2\kappa \left(\frac{p_n^1 - p_n^0}{\Delta r^2} \right)$. Here we applied the same boundary conditions, $\partial_r c(0) = \partial_r p_r(0) = 0$ and l'Hospital's Rule to resolve the singularity at $i = 0$. At $i = N-1$, the boundary condition $\sigma_{rr}(R) = 0$ gives the value of the ghost point $u_n^N = u_n^{N-2} - \frac{2\Delta r}{B+G} \left[(B-G) \left(\frac{u_n^{N-1}}{R} \right) + \beta \log \left(\frac{(c_n^{N-1})}{c_0} \right) \right]$ in Eqs. (22) and (23). The boundary condition $\partial_r c(R) = 0$ gives the value of the ghost point $c_n^N = c_n^{N-2}$ in Eqs. (22), (23) and (24) while the boundary condition $\partial_r p_r(R) = 0$ gives the value of the ghost point $p_n^N = p_n^{N-2}$ in Eq. (24). Eqs. (22), (23) and (24) are then integrated numerically with the given initial and boundary conditions, using the Runge–Kutta–Fehlberg method.

Model parameters. While the model parameters are cell-type dependent, they are chosen so as to quantitatively reproduce our experimental data on MDCK cell monolayers for traction, velocity and intercellular stress. Specifically, the radius of the cell monolayer is taken to be $R = 350 \, \mu$m and the values of the elastic moduli, B and G, and the contractile stress β are taken to be of the same order of magnitude with the experimentally measured effective elastic modulus K of the monolayer. The values of the timescales regulating the chemical dynamics, τ and α^{-1}, are tuned so as reproduce the experimentally measured time period of oscillations $\sim$6 hrs. The remaining values are chosen within the order of magnitudes reported in prior literature. A complete list of the parameter values is given in Supporting Table S1.

Experimental validation of the model predictions.

- *Contractile activity generates effective elasticity and mechanical waves.* Our model predicts that the coupling between contractility and the monolayer strain yields an effective bulk modulus, $K = B + \alpha\tau(\beta + fw/2ah)$ that is greater than the passive bulk elastic modulus of the material (13). Furthermore, in our model waves arise due to a local feedback between rate of production of c and mechanical strain in the monolayer. This is consistent with our experimental data which shows that the treatment with blebbistatin (an inhibitor of myosin-based contractility) reduces the effective elastic modulus K of the cell monolayer by an order of magnitude and eliminates the waves (Fig. 4 a–d).

6

Supporting Table S1: Model parameters.

Parameter	Physical Meaning	Numerical Value
ζ	Viscous friction with the substrate	0.2 Pa hr/μm
f	Propulsion force	10 Pa
R	Monolayer radius	350 μm
h	Monolayer thickness	3 μm
B	Bulk elastic modulus	300 Pa
G	Shear elastic modulus	200 Pa
β	Magnitude of the active stress	600 Pa
τ	Timescale of relaxation of c	1.17 hrs
α	Rate of production of c due to cell stretching	2.14 hr^{-1}
a	Rate of relaxation to a homogeneously polar state	0.78 hr^{-1}
κ	Stiffness constant characterizing the cost of local changes in $\mathbf{p}$	8.75 μm^2/min
w	Controls the rate of alignment of $\mathbf{p}$ with the gradients of c	2.08 μm/min

- *Cell polarization aligns with the gradients of contractile tension.* Our minimal model incorporates feedback between $\mathbf{p}$ and c such that $\partial_t \mathbf{p} \propto \nabla(c/c_0)$. Because the active stress σ_a goes as $\log(c/c_0)$, we expect that $\partial_t \mathbf{p} \propto \nabla\sigma$. Furthermore, since $\mathbf{T} = \zeta\mathbf{v} - f\mathbf{p}$, and $\mathbf{v}$ averages to 0 over one period of oscillation, we expect that $\langle\partial(-\mathbf{T})/\partial t\rangle \sim \langle\nabla\sigma\rangle$, where the angular brackets denote time average over one period of oscillations. When we compare directions of $\langle\partial(-\mathbf{T})/\partial t\rangle$ and $\langle\nabla\sigma\rangle$, we find alignment (Supporting Fig. S10).

- *Cell polarization exists even in the absence of contractility.* Our experimental data show that after treatment with blebbistatin, the traction and the velocity field of the monolayer are misaligned on average, with the traction vectors pointing radially inward at the perimeter of the island and cell motion polarized radially outwards (Supporting Fig. S11). This behavior of cells to polarize their motion radially outward is consistent with the results of the *u–p model* that reproduces the anti-alignment between traction and velocity in the absence of contractility (Supporting Fig. S6 d,e).

- *Scaling of the time period with monolayer size.* A linear stability analysis of our continuum model predicts a characteristic frequency of oscillatory waves in the monolayer given by (13),
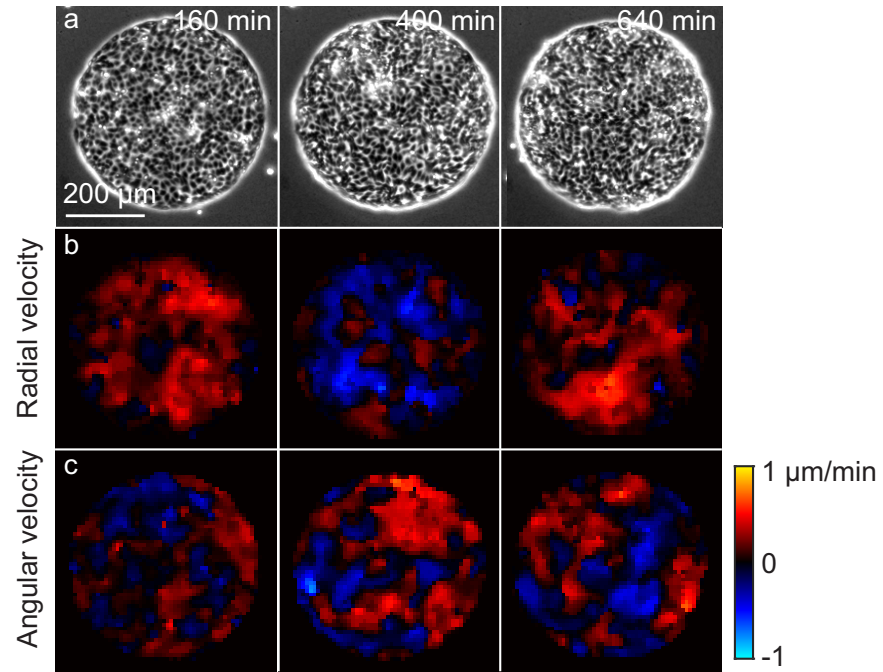
$$\omega_0(q) \simeq q\sqrt{hK/\tau\zeta}\,, \tag{25}$$

where q is the radial wave vector. At length scales comparable to the monolayer size, $q \simeq 1/R$, we get the following analytical expression for the time period,

$$T \simeq 2\pi R\sqrt{\tau\zeta/hK}\,. \tag{26}$$

Our model thus predicts a linear scaling relation between the time period of oscillations and the monolayer radius, in agreement with experimental measurements (7).
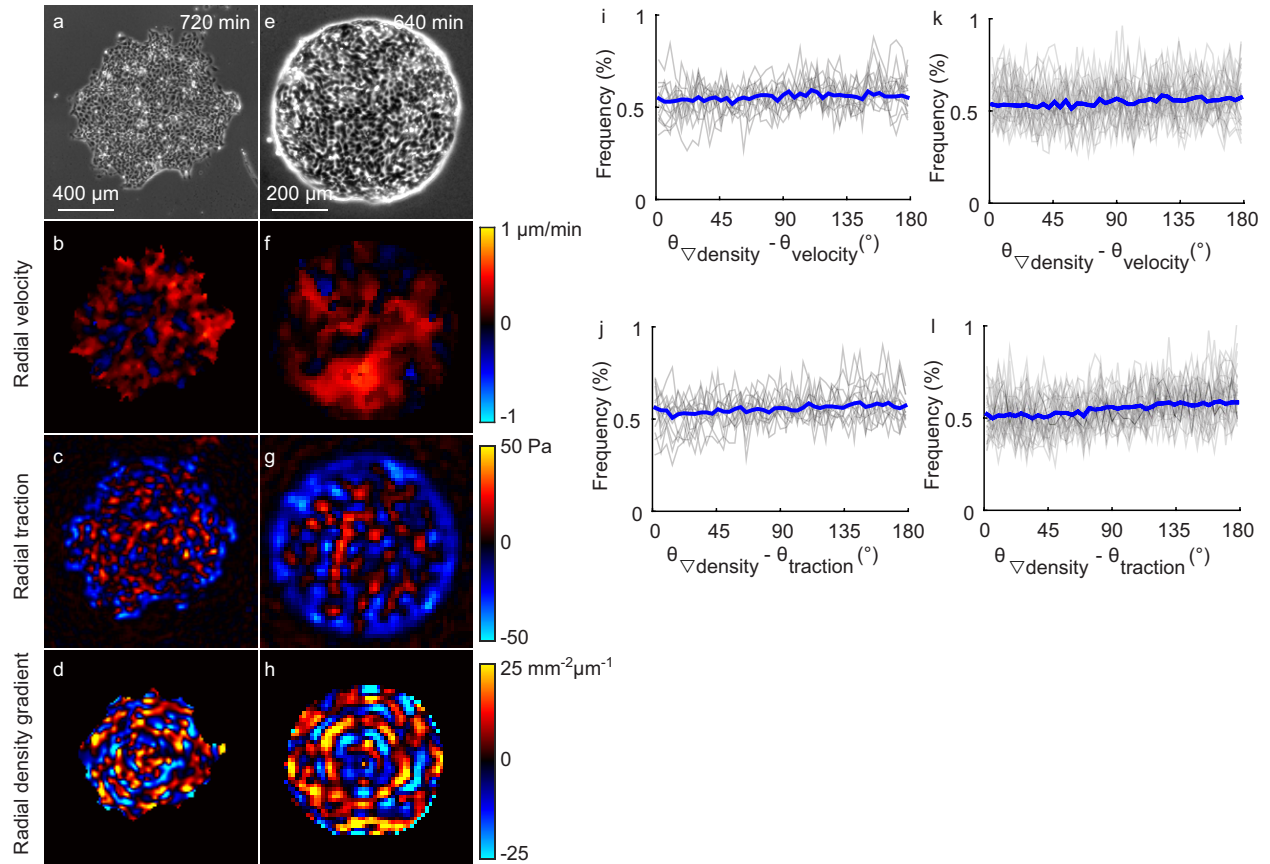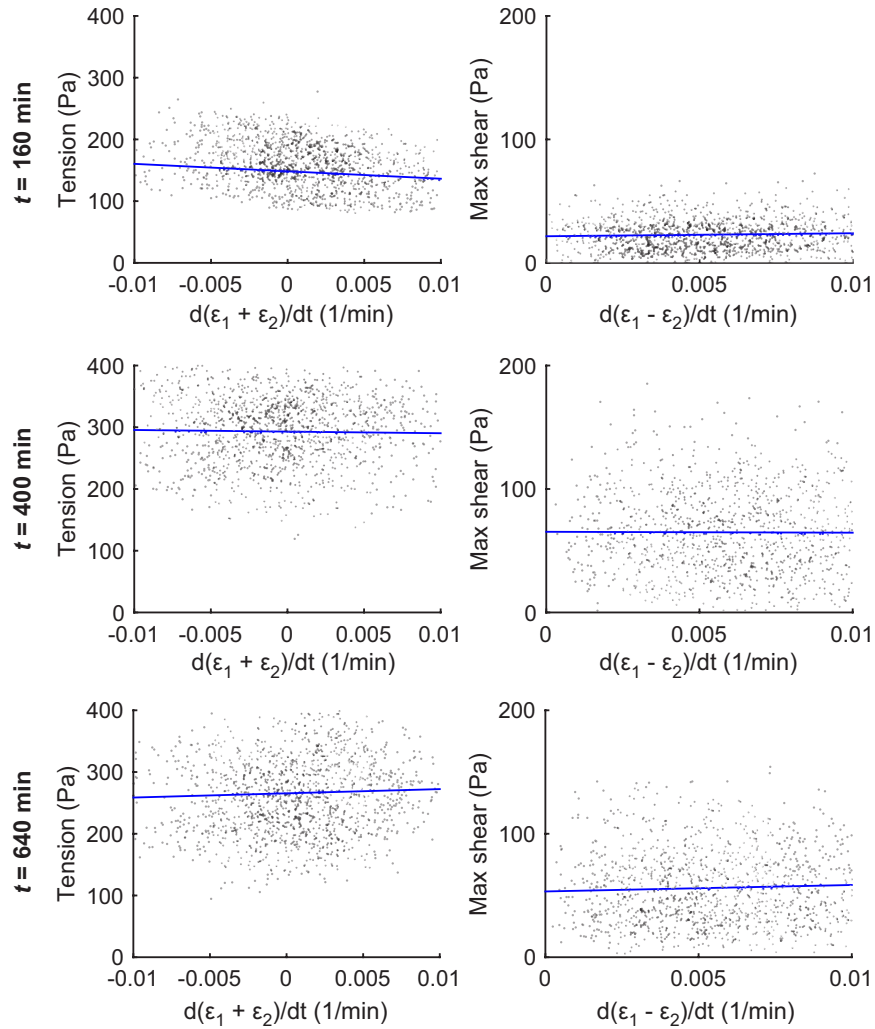
Supporting Figures

Supporting Figure S1: Full velocity field of the the monolayer shown in Fig. 1. (a) Phase contrast images at three different time points. (b, c) Radial (b) and angular (c) components of the cellular velocity.
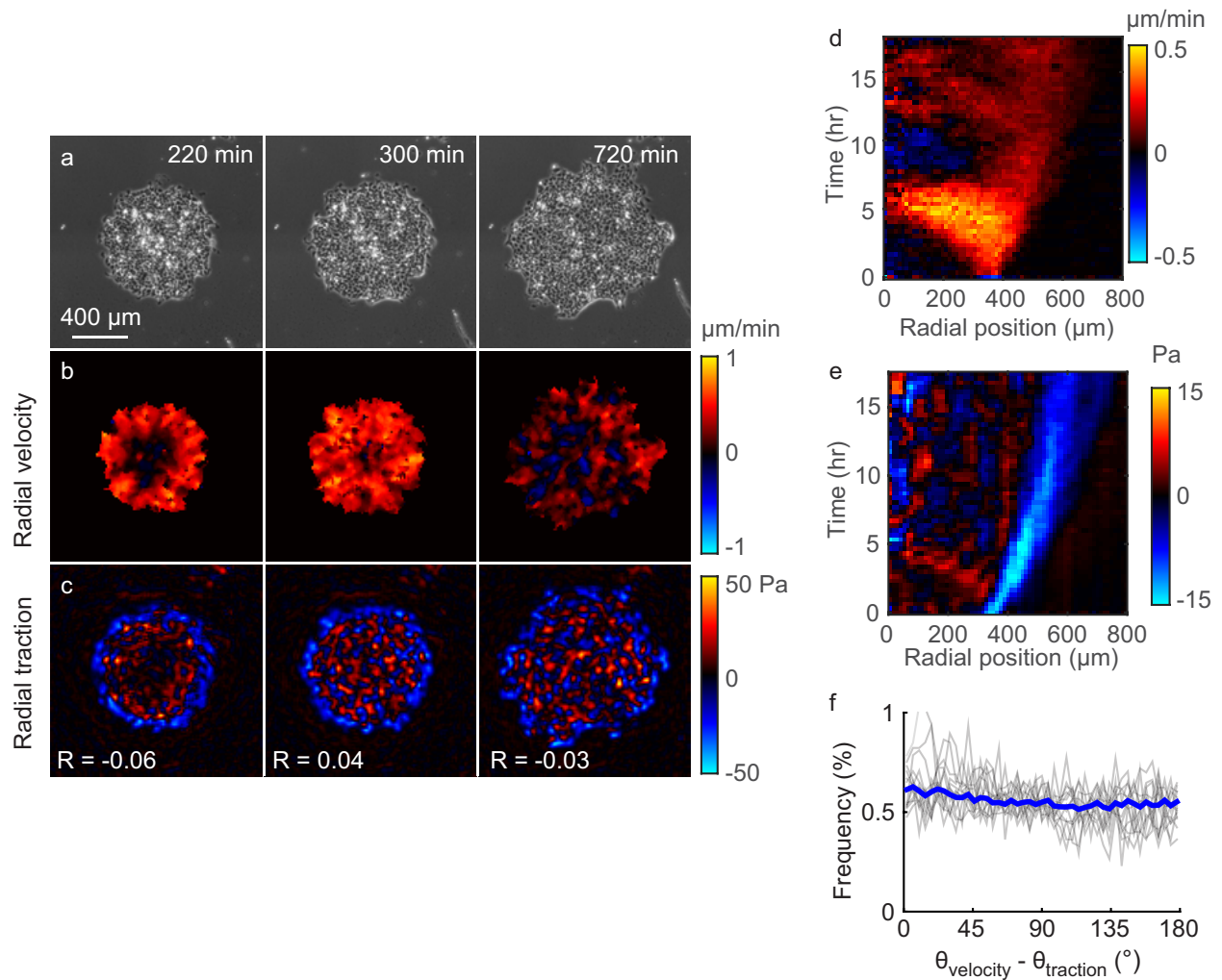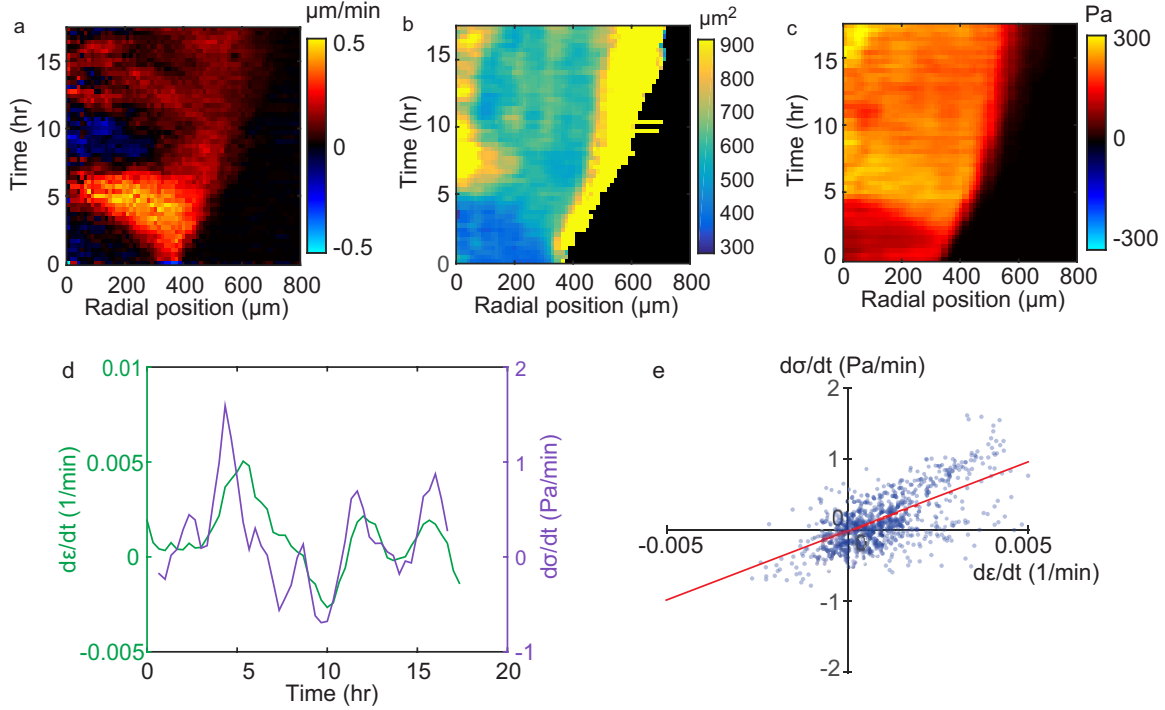
Supporting Figure S2: In expanding cellular monolayers, cellular tractions align in a different direction than cellular velocities. (a) MDCK cells are micropatterned into 700 μm islands using a PDMS mask on a polyacrylamide gel. When the mask is removed, the cells migrate outward. Times are in minutes after removing the mask. (b) Cell velocities are measured using particle image velocimetry, and the radial component of the velocity vector is plotted. The positive direction (red) represents outward motion. At early times (220 min), cells at the periphery move outward; later (300 min), all cells move outward. Once the island is fully spread (720 min), cells move either inward or outward. (c) Radial component of traction applied by the cells to the substrate. Areas in blue indicate regions where the cells pull inward on the substrate; this inward force, if unbalanced, would accelerate the cells outward. The relationship between velocity and traction is evaluated with Pearson's correlation coefficient, R. (d, e) Kymographs of radial velocity (d) and radial traction (e). At all points in time, neither the spatial map of tractions (c) nor the averaged tractions (e) correlate with the velocity. (f) Histogram of the angle between the velocity and traction vectors. Each gray line shows a single point in time for the cell island; the blue line shows all points in time.

Supporting Figure S3: Gradients in local number density do not drive collective motion in expanding or confined monolayers. (a) Phase contrast image of MDCK cells in an expanding island 720 min after removing the mask. (b–d) The radial components of velocity (b) and traction (c) are uncorrelated with the radial component of the density gradient (d) (Pearson's correlation coefficient R = -0.06 and 0.07, respectively). (e–h) For a confined monolayer (e), radial velocity (f) and radial traction (g) are similarly uncorrelated with the radial component of density gradient (h) (Pearson's correlation coefficient R = 0.03 and -0.12, respectively). (i–l) Histograms of the angle between the directions of density gradient and velocity (i, k) or density gradient and traction (j, l) for the expanding (i, j) or confined (k, l) islands. Each gray line shows the histogram for a single point in time for a cell island; the blue lines show histograms for all points in time. Computation of all density gradients reports data points located at least 50 μm from the boundary of the cell island so as to avoid errors in computing the density gradient near the outside of the island where density is zero.

Supporting Figure S4: Negligible viscous stress in the monolayer. To investigate the role of viscosity in the monolayer, the tension (defined as the mean of the principal stresses) is compared to the sum of the principal strain rates, and the maximal shearing stress (defined as half the difference of the principal stresses) is compared to the difference of the principal strain rates. The data shown is for the cell island of Fig. 1 at time points 160, 400, and 640 min. Each dot represents a different location in the island; the blue lines show linear fits. Correlation coefficient magnitudes are typically smaller than 0.1, indicating viscosity has a negligible contribution to the stress tensor.

Supporting Figure S5: The elasticity of the monlayer is tested using an expanding island of MDCK cells. (a) As shown in the kymograph of radial velocity, when a circular island of cells expands outward, a wave of motion propagates from the periphery to the interior. (b) Kymograph of cell area showing area increases when each cell begins to move. (c) Kymograph of tension shows tension within each cell increases as area increases. (d) A trace of the kymographs of area strain rate $d\varepsilon/dt$ (defined as the trace of the rate-of-strain tensor) and time derivative of tension $d\sigma/dt$ along a radial position of 100 μm shows a correlation (Pearson's correlation coefficient $R = 0.67$). (e) A scatter plot of all points in space and time for this monolayer shows $d\sigma/dt$ is correlated with $d\varepsilon/dt$ ($R = 0.64$), indicating elastic behavior with a modulus K (given by the slope of a linear fit) of 71 Pa for this cell island. An average over 8 cell islands gives $K = 62 \pm 17$ Pa (mean $\pm$ standard deviation).
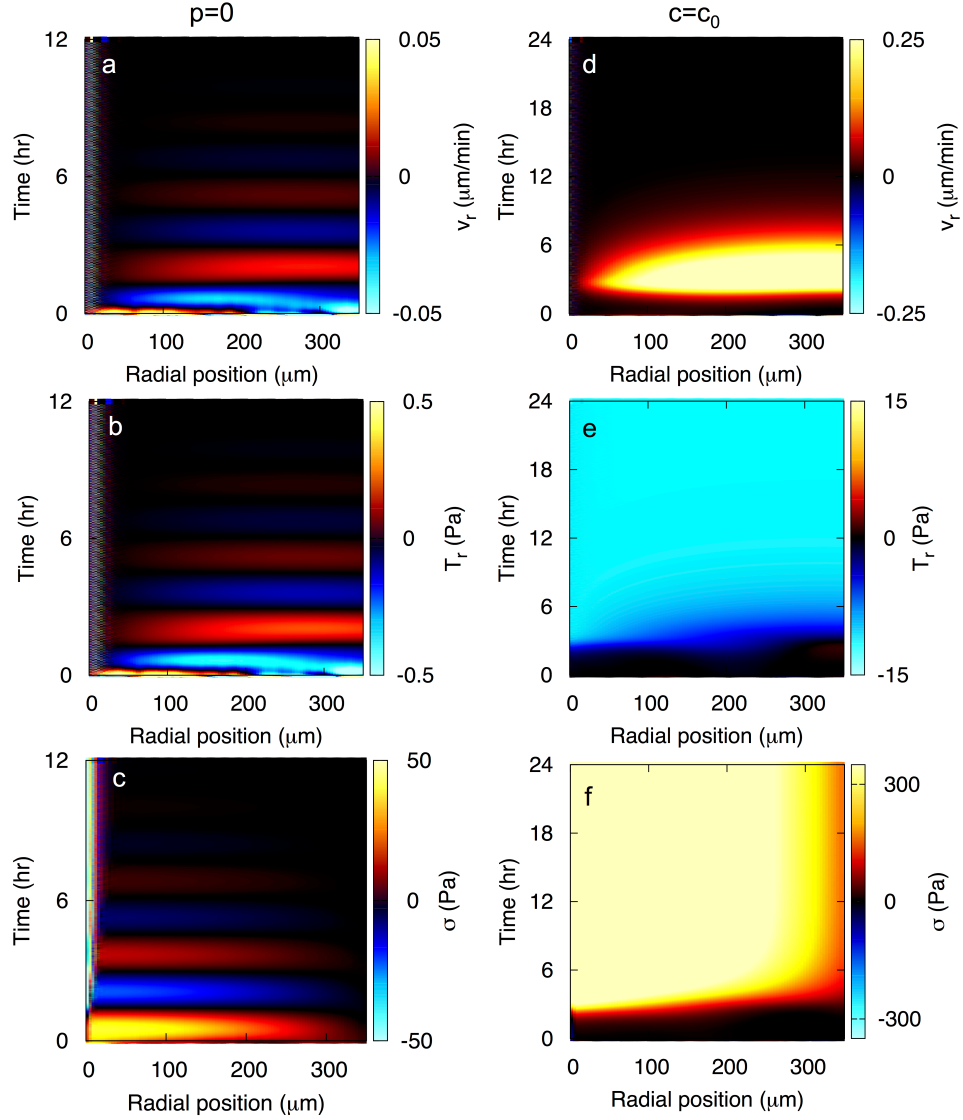
Supporting Figure S6: Limiting cases of the minimal physical model. (a–c) **u**-*c* model: Deformation **u** is coupled to *c* only. The polarization field **p** is set to zero and $\tau = 0.12$ hrs. Rest of the parameters are the same as in Supporting Table S1. In this case we obtain standing waves seen in the kymograph of velocity (a) qualitatively similar to our experiments. However, the traction (b) is proportional to velocity and is very different from the traction observed in our experiments. The monolayer tension (c) oscillated out of phase with velocity with both positive and negative values in disagreement to our experimental data. (d–f) **u**-**p** model: Deformation **u** is coupled to **p** only with the concentration field *c* set to its equilibrium value c_0. Simulation parameters are the same as in Supporting Table S1. In this case no wave-like behavior is obtained, indicating that the feedback between mechanical strain and the regulatory biochemistry of *c* is essential to explain the presence of wave-like dynamics.

13
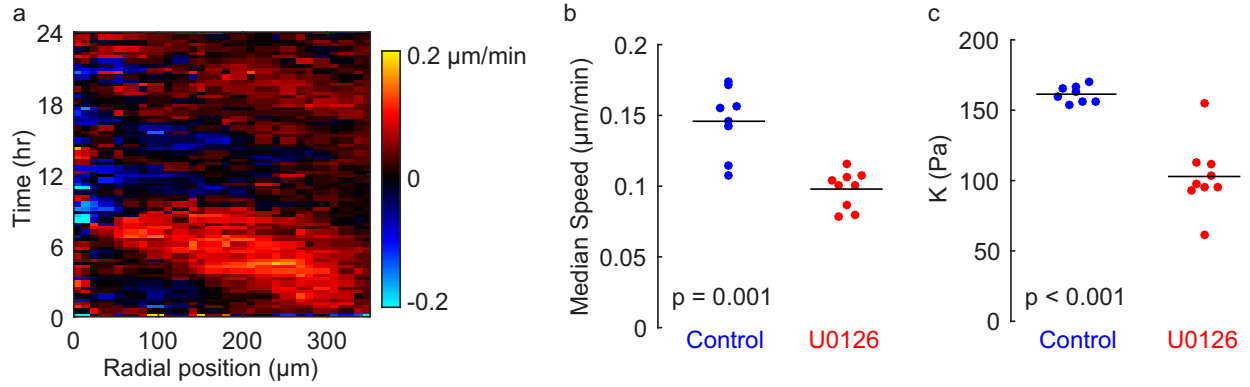
Supporting Figure S7: ERK inhibition. The ERK inhibitor U0126 (10 µM) decreases the velocity and eliminates the waves. (a) Kymograph of velocity shows no waves of cellular motion are present. (b) Compared to control, cell islands treated with U0126 move at a slower speed. (c) Compared to control, treatment with U0126 reduces the elastic modulus K. For the plots in (b) and (c), each dot corresponds to a different cell island. P values are computed using a rank sum statistical test.
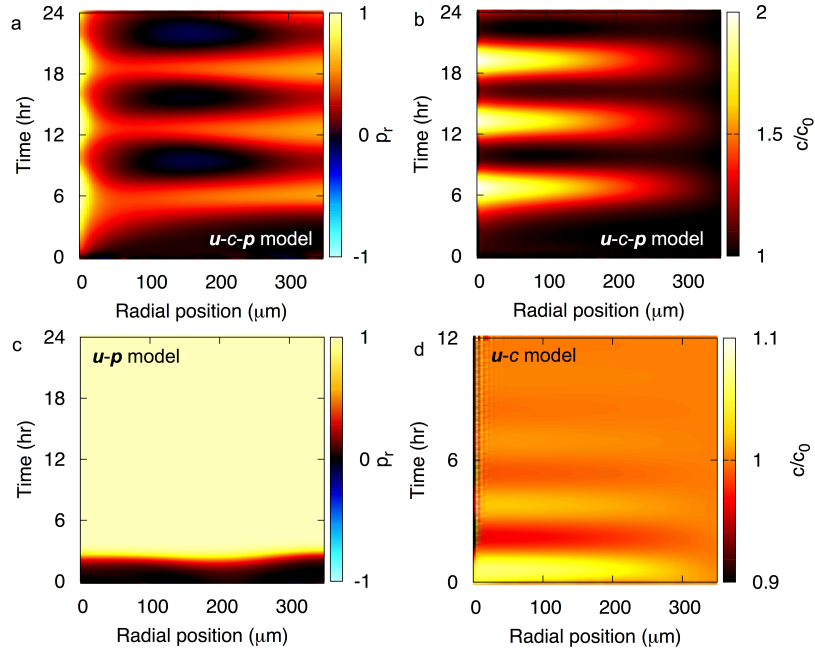

Supporting Figure S8: Dynamics of the internal state variables in the cell monolayer. (a) Kymograph of the polarization field in the full **u**-c-**p** model shows that cells at the boundary and at the center of the monolayer are polarized outwards separated by a band of inward polarized cells. (b) Kymograph of the concentration field in the full **u**-c-**p** model showing oscillations similar to the monolayer tension. (c) In the absence of coupling to c, the polarization field is uniform and points radially outward. (d) Kymograph of the concentration field in the absence of coupling to polarization field.
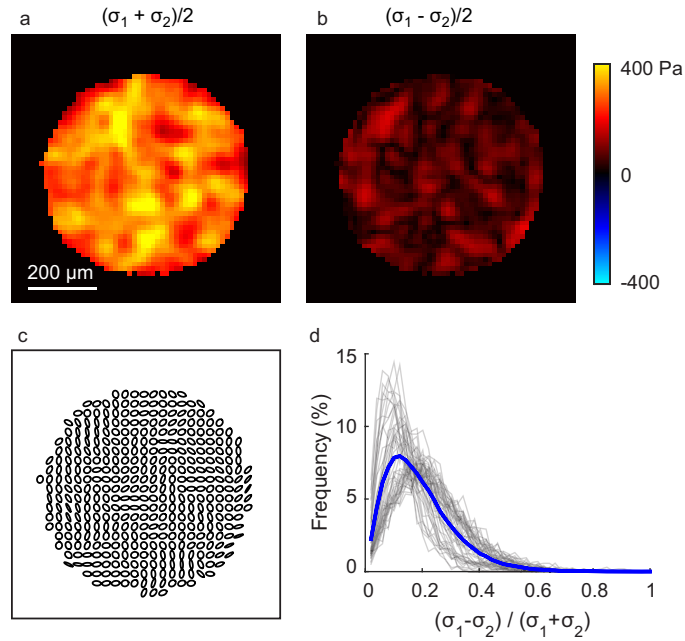
Supporting Figure S9: The stress tensor within the circular monolayers is isotropic. The first and second principal stresses, σ_1 and σ_2, are computed. (a, b) Representative plots of the mean principal stress, $(\sigma_1 + \sigma_2)/2$ (a) and the maximum shear stress, $(\sigma_1 - \sigma_2)/2$ (b) for a circular monolayer at one point in time. (c) Visualization of the stress tensor in the monolayer where the major and minor axes of each ellipse correspond to the magnitude of σ_1 and σ_2, and the orientation of the major axis corresponds to the orientation of the first principal stress σ_1. An ellipse that is more circular indicates a stress tensor that is more isotropic. (d) As a measure of stress isotropy, the difference in the principal stresses is divided by the sum of the principal stresses with a value of zero indicating a fully isotropic state. Histograms of $(\sigma_1 - \sigma_2)/(\sigma_1 + \sigma_2)$ are generated for each point in time (gray lines) and for all time points (blue line). The mean and median are <0.2, indicating the stress tensor is nearly isotropic.
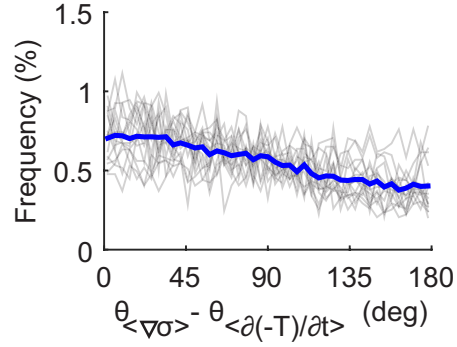
Supporting Figure S10: Cells polarize along gradients of contractility. The difference in the orientations of the gradient of tension, $\theta_{\langle\nabla\sigma\rangle}$, and the opposite of the time derivative of traction, $\theta_{\langle\partial(-\mathbf{T})/\partial t\rangle}$, is plotted as a histogram for various points in time (gray lines) and for all time points (blue line). Here, the angle brackets represent a time average over one period of oscillation. The peak near zero indicates that directions of $\langle\nabla\sigma\rangle$ and $\langle\partial(-\mathbf{T})/\partial t\rangle$ tend to align, in agreement with the model. The alignment between directions of $\langle\nabla\sigma\rangle$ and $\langle\partial(-\mathbf{T})/\partial t\rangle$ means that the cell tractions evolve in time so as to propel the cells towards regions of high tension.
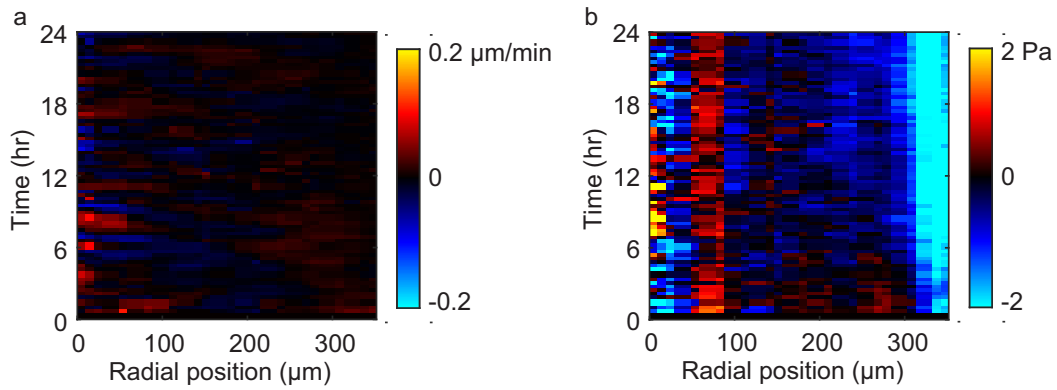

Supporting Figure S11: Blebbistatin treatment. Kymographs of (a) radial velocity and (b) radial traction for a cell island treated with blebbistatin (20 μM). The tractions are generally aligned in the opposite direction as the radial velocity. The observed anti-alignment agrees with the model when contractility is inhibited (Supporting Fig. S6 d–f). In this figure, panel (a) is the same as Fig. 4a.
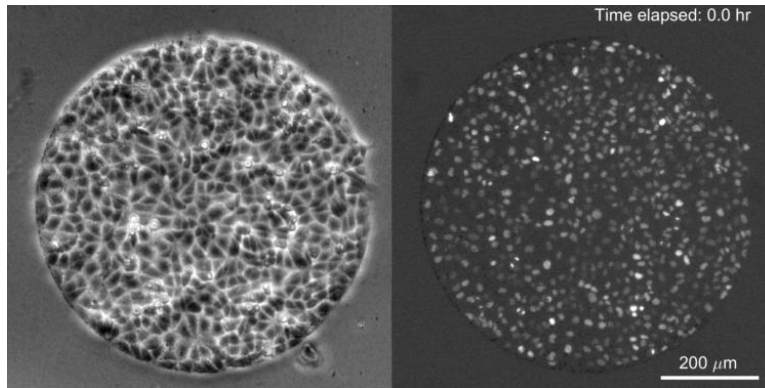
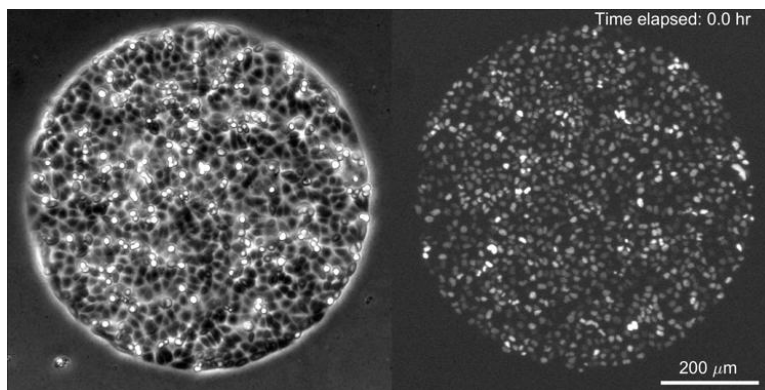# Supporting Movie Legends
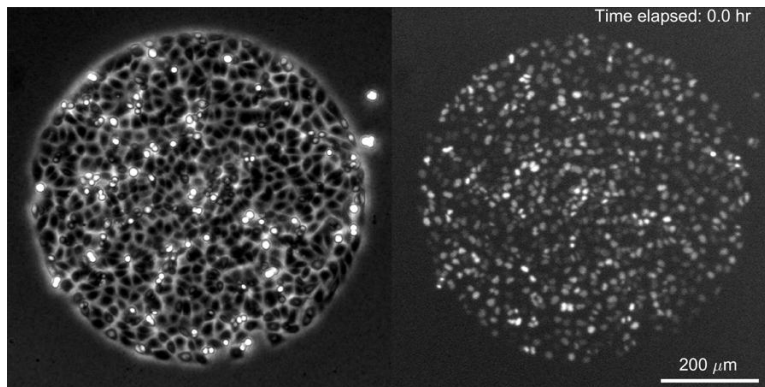
Supporting Movie 1: Oscillations of motion in a cell monolayer. Left: phase contrast; right: nuclei expressing green fluorescent protein.
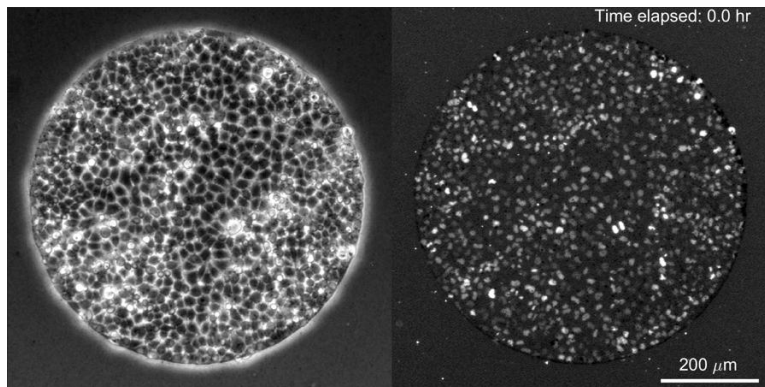
Supporting Movie 2: Motion of a cell monolayer treated with blebbistatin. Left: phase contrast; right: nuclei expressing green fluorescent protein.

Supporting Movie 3: Motion of a cell monolayer treated with EGF. Left: phase contrast; right: nuclei expressing green fluorescent protein.

Supporting Movie 4: Motion of a cell monolayer treated with U0126. Left: phase contrast; right: nuclei expressing green fluorescent protein.